https://doi.org/10.5194/egusphere-2026-2293
Preprint. Discussion started: 24 June 2026

A mountain-generated mesoscale test case from DCMIP-2025: Gap flow and vortex shedding variants

Timothy C. Andrews[1], Christiane Jablonowski[1], Owen K. Hughes[1], and Thomas M. Bendall[2]

[1]Department of Climate and Space Sciences and Engineering, University of Michigan, Ann Arbor, MI, USA
[2]Dynamics Research, Met Office, Exeter, United Kingdom

Correspondence: Timothy C. Andrews (timand@umich.edu)

Abstract. DCMIP-2025, the fourth instance of the Dynamical Core Model Intercomparison Project (DCMIP), introduced new test cases for the evaluation of dynamical cores for atmospheric General Circulation Models. This paper overviews one of these test cases focused on mesoscale dynamics generated by mountain orography, using simple initial conditions and varying surface profiles to produce nonlinear flows. This work investigates two orographies: a mountain chain that instigates a gap flow, and an isolated mountain which generates vortex shedding. These tests are used to compare four state-of-the-art dynamical cores: CAM-SE (spectral element), CAM-FV3 (finite volume cubed-sphere), and CAM-MPAS (Model for Prediction Across Scales) from NCAR's Community Atmosphere Model (CAM), along with GungHo, the dynamical core from the UK Met Office's new LFRic model. Simulation comparisons highlight the impact of model features such as the mesh and sources of numerical diffusion. This test, with its two variants, adds to the existing suite of cases that enable the rigorous examination and comparison of dynamical cores.

1 Introduction

Atmospheric General Circulation Models (GCMs) are highly complex systems, containing many components that must work well in isolation and in combination for an accurate simulation. At the heart of these models lies the dynamical core, which updates the dynamical state by solving an approximation to the compressible Euler equations on the sphere. The governing dynamical equations are challenging to solve for a number of reasons, including the wide range of temporal and spatial scales and the presence of nonlinearities. This means that even when considering solely the dynamical core in a dry, adiabatic atmosphere with no physical parametrisations, evaluating its accuracy and behaviour is a demanding task.

An informative approach for evaluating dynamical cores is the application of idealised test cases. Even in the absence of analytical solutions, simulations can be compared to expected behaviour from physical arguments or a high-resolution reference solution. Test cases can expose errors in the numerical algorithms, such as in Williamson et al. (2009) and Park et al. (2013). The efficacy of test cases motivated the creation of the Dynamical Core Model Intercomparison Project (DCMIP). In DCMIP

https://doi.org/10.5194/egusphere-2026-2293
Preprint. Discussion started: 24 June 2026

events, a number of idealised initial conditions are run with different dynamical cores to contrast the impact of specific model decisions, such as the computational mesh, spatial discretisation, horizontal and vertical grid staggerings, transport scheme, and diffusion mechanisms. The first DCMIP meeting was held in 2008 (Jablonowski et al., 2008), with subsequent events in 2012 (Ullrich et al., 2012) and 2016 (Ullrich et al., 2017, 2016). Many DCMIP tests are widely used in the dynamical core community, including baroclinic wave (Jablonowski and Williamson, 2006; Ullrich et al., 2014), tracer transport (Kent et al., 2014), terminator toy chemistry (Lauritzen et al., 2015), supercell (Zarzycki et al., 2019), and tropical cyclone (Willson et al., 2024) cases.

The fourth DCMIP event, held in June 2025, introduced new test cases focused on mesoscale and nonhydrostatic moist dynamics, along with the evaluation of machine learning models with idealised initial conditions. Excluding the machine learning portion, three dynamical core test cases were developed for DCMIP-2025:

1. Gravity wave breaking, with a focus on the impact of vertical resolution like Skamarock et al. (2019), but with the double mountain orography of Hughes and Jablonowski (2023) and a sharp transition in Brunt-Väisälä frequency at the tropopause.

2. Mountain-generated mesoscale dynamics, with specific orography used to instigate either a gap flow or vortex shedding.

3. A squall line test building off the supercell test case (Zarzycki et al., 2019; Klemp et al., 2015), with multiple temperature perturbations, Kessler microphysics, and a radar reflectivity metric.

This paper describes the second test case and its application to four dynamical cores.

With a push for finer spatial resolutions in weather prediction models (Stevens et al., 2019; Wedi et al., 2020), such as global 3 km and even 1 km grid spacings, the accurate representation of mesoscale dynamics becomes increasingly important. Lin (2007) defines mesoscale dynamics as that which evolves on a length scale between 20 km and 1000 km, which encompasses a range of dynamics in a GCM. To investigate smaller-scale mesoscale dynamics at coarser horizontal resolutions, our test uses a reduced-radius spherical domain as discussed by Kuang et al. (2005), Wedi and Smolarkiewicz (2009) and others, which we call the small Earth modification.

The initial condition in this test case is described by simple analytic functions, enabling a straightforward implementation in an arbitrary dynamical core. The motivation behind the test case is to probe how the model simulates the effect of orography in constructing mesoscale dynamics. Although there are some dynamical core test cases on the sphere that feature orography, e.g. mountain Rossby waves in Tomita and Satoh (2004) and baroclinic instability in Hughes and Jablonowski (2023), we note that the majority of tests use a constant surface height. Hence, more tests with orography would be beneficial for a more comprehensive evaluation of dynamical cores. Our use of a small Earth leads to steep orographies, so this test may highlight model deficiencies in the presence of large surface height gradients, in preparation for moving towards finer horizontal resolutions.

The first choice of orography instigates a gap flow, which is typically observed through a mountain chain or strait. Real-world examples of gap flow are the Chivela pass in Mexico (≈100 km wide gap) (Steenburgh et al., 1998; Cherrett, 2006; Hong et al.,

https://doi.org/10.5194/egusphere-2026-2293
Preprint. Discussion started: 24 June 2026

2018), the Shelikov Strait in Alaska (≈40–48 km wide) (Liu et al., 2006), the Juan de Fuca straight between the United States and Canada (≈18–27 km wide) (Reed, 1931; Overland and Walter Jr, 1981), and the Cook Strait in New Zealand (≈20 km wide at its narrowest point) (Reid, 1996). Higher resolution models can better represent the strong accelerations through gaps; an example is the strong gap winds detected through the Chivela pass in Zarzycki et al. (2015) when moving to a regionally refined mesh over the North Atlantic. Previous numerical studies of gap flow include idealised orography in Gaberšek and Durran (2004) and Zängl (2002), and specific orographies of the Alps in Mayr et al. (2007) and the Juan de Fuca Strait in Colle and Mass (2000).

The second orography variant leads to vortex shedding, which is typically observed downstream of islands. Atmospheric vortices are closely related to von Kármán vortex streets, as first discussed by Hubert and Krueger (1962) and subsequent observational studies (Chopra and Hubert, 1964, 1965; Tsuchiya, 1969). An analogous vortex shedding in the oceans occurs in island wakes, e.g. (Dietrich et al., 1996; Dong and McWilliams, 2007; Pattiaratchi et al., 1987). Whilst classical von Kármán vortex streets are generated by the separation of a viscous boundary layer, different mechanisms drive the formation of atmospheric vortex streets, with proposed theories being the inviscid tilting of horizontal vorticity (Smolarkiewicz and Rotunno, 1989), or diffusion and a lack of potential vorticity conservation (Smith, 1989a; Schär and Smith, 1993; Schär and Durran, 1997). Recent observational studies of atmospheric vortex streets include Horváth et al. (2020), Wu et al. (2025) and Liu et al. (2023). Increased computational resources in recent years have allowed for more comprehensive numerical studies, such as the one-kilometre resolution and ten-year climatology in Gao et al. (2023) for Madeira Island. Previous numerical studies of vortex shedding that informed our test case variant are Schär and Durran (1997) and Sun and Chern (1994).

To our knowledge, this test case from DCMIP-2025 is the first time that gap flow and vortex shedding phenomena have been used to investigate the performance of dynamical cores. Many numerical studies of gap flow and vortex shedding neglect the Coriolis force, or use f- or β-plane approximations, such as in Sun and Chern (1994). Our test is run both with and without rotation, with the former using the full Coriolis parameter, to examine the impact of a rotational force on the mesoscale dynamics. Additionally, where many previous numerical studies used a Cartesian domain, we work with the standard spherical approximation of the Earth.

Four dynamical cores participated in DCMIP-2025: three models from the United States that are accessible through the Community Atmosphere Model (CAM) (Neale et al., 2010), developed by the National Center for Atmospheric Research (NCAR) — the spectral element model (SE) (Lauritzen et al., 2018), the finite volume cubed-sphere model (FV3) from NOAA's Geophysical Fluid Dynamics Laboratory (GFDL) (Harris et al., 2021), and the Model for Prediction Across Scales (MPAS) from NCAR (Skamarock et al., 2025). The other tested model was GungHo (Melvin et al., 2024), the dynamical core used in the UK Met Office's next-generation LFRic-Atmosphere model. Due to differences in model design, there are distinct variations in the gap flow and vortex shedding simulations from each dynamical core. Specifically, the sources and strengths of explicit and implicit diffusion have a significant impact, and we will briefly examine the sensitivity of one such mechanism within each model.

In the next section, the initial condition for the test case is described, along with the vertical grid and a Rayleigh damping subdomain for reducing wave reflections from the model top. Section 3 details the design choices of the four dynamical cores.

https://doi.org/10.5194/egusphere-2026-2293
Preprint. Discussion started: 24 June 2026

Section 4 describes the gap flow variant and compares simulations from the dynamical cores, whilst section 5 does the same for the vortex shedding variant. Section 6 then compares the effect of a diffusion modelling choice in each dynamical core in this test case. Section 7 ends the paper with conclusions from the simulations and a discussion of possible test case modifications and future numerical experiments.

2 General test case information

2.1 Initial condition

We present the initial condition using the fields that are required to initialise the Community Atmosphere Model (CAM), which are the zonal wind (u), meridional wind (v), temperature (T), surface geopotential ($\Phi_\mathrm{s} = g z_\mathrm{s}$, where z_s is the surface height and g is gravity) and surface pressure (p_s). The surface geopotential and surface pressure are two-dimensional fields defined in longitude-latitude (lon-lat) coordinates, with longitude $\lambda \in [0, 2\pi)$ and latitude $\phi \in [-\pi/2, \pi/2]$. The horizontal wind components and temperature are three-dimensional fields that are initialised on each pressure level. As there is no vertical variation in the initial condition, the analytic expressions are identical with other choices of vertical coordinate, i.e. height. Additionally, a non-zero vertical velocity can be initialised with nonhydrostatic models, which will be discussed later.

The initial condition specifies an isothermal atmosphere, balanced surface pressure, and a zonal wind corresponding to a solid-body rotation,

$$u(\lambda, \phi, p, t = 0) = u_0 \cos(\phi), \tag{1a}$$

$$v(\lambda, \phi, p, t = 0) = 0, \tag{1b}$$

$$T(\lambda, \phi, p, t = 0) = T_0, \tag{1c}$$

$$\Phi_\mathrm{s}(\lambda, \phi) = g z_\mathrm{s}(\lambda, \phi), \tag{1d}$$

$$p_\mathrm{s}(\lambda, \phi, t = 0) = p_\mathrm{sp} \exp\left[-\frac{a N^2 u_0}{2 g^2 \kappa} \left(\frac{u_0}{a} + 2\Omega \right) \left(\sin^2(\phi) - 1 \right) - \frac{N^2}{g^2 \kappa} \Phi_\mathrm{s} \right], \tag{1e}$$

with the parameters defined in Table 1. The surface height of $z_\mathrm{s}(\lambda, \phi)$ encodes the orography and is the only point of difference between the gap flow and vortex shedding variants. The gap flow test uses a mountain chain with a maximum height of $h_0 = 1500$ m, and the vortex shedding test uses an isolated Gaussian mountain with a height of $h_0 = 2000$ m. The orographies will be explicitly stated in the gap flow and vortex shedding test descriptions (Sect. 4 and 5), with both constructed from exponential functions so that $z_\mathrm{s}(\lambda, \phi) \in \mathcal{C}^\infty$. This allows the orography to be well represented on the computational mesh and simplifies the derivation of nonzero initial vertical velocities for nonhydrostatic dynamical cores (Appendix A). The surface pressure (1e) is constructed such that $dv/dt = 0$, which leads to a similar expression to the mountain-induced Rossby wave test from DCMIP-2008 (Jablonowski et al., 2008), which was later used to test the MCore model in Ullrich and Jablonowski

https://doi.org/10.5194/egusphere-2026-2293
Preprint. Discussion started: 24 June 2026

(2012) [1]. The initial surface pressure reflects the absence or presence of the Coriolis force, as shown in Figure 1 with the gap flow orography. For z-coordinate models that require an initial pressure along each height level, the three-dimensional pressure field in the isothermal atmosphere is computed as

$$p(\lambda, \phi, z, t = 0) = p_{\mathrm{s}} \exp\left(\frac{-g(z - z_{\mathrm{s}})}{R_{\mathrm{d}} T_0}\right). \tag{2}$$

Additionally, some models may require an initial density field, which can be computed using the equation of state.

Table 1. General setup parameters for the mountain-generated, mesoscale flow test case from DCMIP-2025.

Parameter	Definition	Value
X	Small Earth factor	20
u_0	Maximum zonal wind at the equator	10 m s^{-1}
T_0	Isothermal temperature	288 K
g	Earth's gravity	9.80616 m s^{-2}
a	Mean radius of the small Earth	$X^{-1} \cdot 6.371229 \times 10^6$ m
c_{p}	Specific heat capacity at constant pressure	1004.64 J kg $^{-1}$ K^{-1}
R_{d}	Ideal gas constant for dry air	287.04 J kg^{-1} K^{-1}
κ	$R_{\mathrm{d}}/c_{\mathrm{p}}$	2/7
p_{sp}	Pressure at the South pole, i.e. where $\Phi_{\mathrm{s}} \approx 0$ m^2 s^{-2}.	10^5 Pa
Ω	Angular velocity of the Earth, using the sidereal day	$X \cdot 7.2921 \times 10^{-5}$ rad s^{-1}
N	Brunt-Väisälä frequency	≈ 0.0182 s^{-1} (Eq. 3)

Whilst the vertical velocity is diagnosed in hydrostatic dynamical cores, w or an equivalent quantity becomes a prognostic variable in a nonhydrostatic model, and thus requires an initial condition. For a constant surface height, an initial condition of $w(\lambda, \phi, p, t = 0) = 0$ is valid for any vertical coordinate. However, the presence of orography means that $w(\lambda, \phi, p, t = 0) = 0$ violates the impermeability or free-slip boundary condition at the surface. Typically, this imbalance in the model results in the emission of acoustic waves. To obey the surface boundary condition, one can set a nonzero initial vertical velocity. Here, we assume a hybrid or pure terrain-following coordinate and define the initial vertical velocity such that the flow follows the sloped vertical coordinate lines. It is worth noting that this leads to slight variations in the flow between coordinate systems. The derivation of nonhydrostatic vertical velocities with a hybrid z-coordinate is given in Appendix A, along with comparisons of CAM-MPAS simulations with $w(t = 0) = 0$ and $w(t = 0) \neq 0$. We conclude that the use of a nonzero vertical velocity in

[1] Note that this paper contains a typo in Eq. (120), which should be $N = \sqrt{g^2/(c_{\mathrm{p}} T_0)}$. Also, Eq. (121) should be $z_{\mathrm{s}} = h_0 \exp(-(r_c/d)^2)$ to define a surface height, as it currently defines a surface geopotential of $\Phi_{\mathrm{s}} = g z_{\mathrm{s}}$.

https://doi.org/10.5194/egusphere-2026-2293
Preprint. Discussion started: 24 June 2026

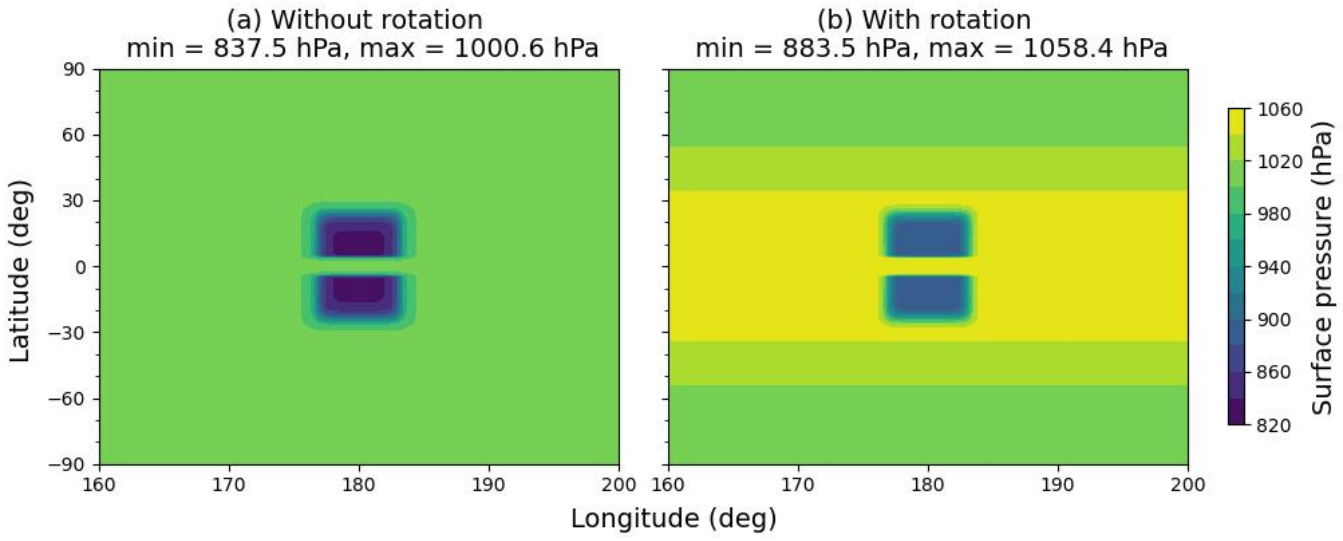

Figure 1. Initial surface pressure fields in the gap flow case without rotation (a) and with rotation (b). These plots use CAM-SE output. The surface pressures are lower over the orography to reflect the increased surface height. Without rotation, the surface pressure has minimal variation with latitude. With rotation, the nonzero value of Ω impacts the pressure field in (1e) to create a larger variation with latitude. Although the maximum surface pressure of 1058 hPa in the case with rotation is on the larger side, tests with a smaller $p_{\text{sp}} = 960$ hPa had minimal impact on the flow dynamics, so we use the same value of $p_{\text{sp}} = 1000$ hPa for both the with and without rotation configurations. Note, for a clearer visualisation of the surface pressure around the orography, an unequal longitude-latitiude aspect ratio is used.

the initial condition does not make a significant impact in this test, where we are focused on low-altitude mesoscale dynamics, so the CAM-MPAS and GungHo simulations presented in the following sections use $w(t = 0) = 0$.

2.2 Nondimensional parameters

We now discuss the key nondimensional parameters used to classify the flow regimes in the test.

With an isothermal initial condition, the Brunt-Väisälä frequency is constant throughout the domain,

$$N = \sqrt{\frac{g^2}{c_{\text{p}} T_0}} \approx 0.0182 \text{ s}^{-1}, \tag{3}$$

which implies that the atmosphere is uniformly, stably stratified.

An important nondimensional number in flows with orography is the inverse Froude number, also termed the nondimensional mountain height (Smith, 1989b; Schär and Durran, 1997),

$$\text{Fr}^{-1} = \frac{NH}{U}. \tag{4}$$

The mountain height and initial wind speed over the centre of the orography are used for the characteristic height (H) and velocity (U) scales. The inverse Froude number quantifies the effect of nonlinearity in the flow downstream of the mountain

https://doi.org/10.5194/egusphere-2026-2293
Preprint. Discussion started: 24 June 2026

(Lin, 2007). A sufficiently small Fr^{-1} leads to the predominantly linear *flow-over* regime. A simple way to make Fr^{-1} smaller is by reducing the orography height; an example is minuscule $h_0 = 1$ m used in the nonhydrostatic test suite of Skamarock et al. (2004) to instigate the linear potential flow regime. With a large enough Fr^{-1}, the flow transitions into the nonlinear *flow-around* regime, which allows for complex dynamics such as wave breaking, flow splitting, or the generation of lee vortices. The transition point from the flow-over to flow-around regime depends on the shape of the orography; this occurs at $\mathrm{Fr}^{-1} = 1.33$ for a circular mountain but at a larger Fr^{-1} for an elliptical orography that extends further in latitude than longitude (for a zonal flow), and at smaller Fr^{-1} for a larger longitudinal extent (Smith, 1989b). Both the gap flow and vortex shedding orographies lead to the nonlinear flow-around regime, and we provide the specific values of Fr^{-1} later.

A key response of this initial condition is the creation of orographic gravity waves, which can be classified as either hydrostatic or nonhydrostatic. The orographic gravity wave regime is determined from the ratio of vertical to horizontal wavelengths (Lin, 2007). The horizontal wavelength is equal to a length scale of L_h, over which one oscillation of a characteristic horizontal wave is contained,

$$\lambda_x = L_\mathrm{h}. \tag{5}$$

The vertical wavelength of the gravity wave is related to the buoyancy and flow velocity through

$$\lambda_z = \frac{2\pi}{l_\mathrm{sc}} = \frac{2\pi U}{N}, \tag{6}$$

where $l_\mathrm{sc} = N/U$ is the Scorer parameter (Scorer, 1949) in the absence of wind shear. The vertical wavelength is independent of the orography, with both test variants instigating gravity waves of $\lambda_z \approx 3450$ m at the equator and reducing λ_z for increasing $|\phi|$. The ratio of the horizontal and vertical wavelengths specifies what we term the *hydrostaticity number* for the orographic gravity waves,

$$\mathrm{Hy} = \frac{\lambda_x}{\lambda_z} = \frac{N L_\mathrm{h}}{2\pi U}. \tag{7}$$

Note that $\mathrm{Hy} = NL/U$ is also used in the literature, e.g. (Dudhia, 1993), with L denoting a characteristic length instead of a terrain wavelength in these cases. If $\mathrm{Hy} >> 1$, then the orographic gravity waves are hydrostatic, with $\lambda_x >> \lambda_z$ causing a nearly directly vertical propagation of the gravity waves. Both tests are in this hydrostatic regime, and so there is expected to be minimal difference between hydrostatic and nonhydrostatic configurations of a dynamical core.

A key feature of the test case is the use of a reduced-radius sphere, which we refer to as the *small Earth modification*. Typically, a small Earth is used to investigate nonhydrostatic regimes without the computational expense of a fine horizontal resolution (Ullrich et al., 2012; Wedi and Smolarkiewicz, 2009; Klemp et al., 2015). We instead use the small Earth modification to construct mountain orographies with more realistic horizontal length scales. Introducing a small Earth factor of $X = 20$ leads to a reduced radius of $a = X^{-1} a_\mathrm{reg} \approx 319$ km, where the 'reg' subscript denotes a quantity on the regular-sized Earth. The timescale of horizontal dynamics is shorter on the small Earth, which requires a rescaling of the timestep size as $\Delta t = X^{-1} \Delta t_\mathrm{reg}$. Another consequence of the small Earth is that *dimensional* explicit diffusion coefficients need to be modified; this is the case for CAM-SE, where the fourth-order hyperviscosity coefficients are scaled by X^{-3}. The divergence damping coefficients in CAM-FV3 are dimensionless, so they are left unchanged.

https://doi.org/10.5194/egusphere-2026-2293
Preprint. Discussion started: 24 June 2026

Both test cases are run with and without the Earth's rotation, with $\Omega = 0$ s^{-1} in the latter instance. Although unphysical, tests without a zero Coriolis parameter are commonly used for dynamical core testing, often when considering small horizontal length scales or the buoyancy-driven vertical slice equations. As most previous studies of gap flow and vortex shedding neglected the Coriolis force, our inclusion of rotational effects enables the exploration of new dynamics.

For tests that include the Coriolis force, the Earth's angular velocity is increased to $\Omega = X\Omega_{\text{reg}}$. This preserves the Rossby number from the regular Earth, which is defined as

$$\text{Ro} = \frac{U}{fL}, \tag{8}$$

where U and L are characteristic velocity and horizontal length scales, and $f = 2\Omega\sin(\phi)$ is the Coriolis parameter. On the small Earth, $L = X^{-1}L_{\text{reg}}$, so we require that $f = Xf_{\text{reg}}$ to enforce $\text{Ro} = \text{Ro}_{\text{reg}}$. Simulations with rotation but without a rescaled Coriolis force will instead generate horizontal dynamics that closely resemble the simulations without rotation. The simulation time is measured in terms of a standard Earth day, approximated as 86400 s, although the small Earth completes twenty revolutions in this duration.

2.3 Vertical grid

An advantage of the simple initial condition (1) is its lack of vertical variation. Hence, the analytical expressions are the same irrespective of the choice of vertical coordinate. We construct a vertical grid with a varied resolution, so that the levels near the orography are better resolved than the upper levels. We describe this vertical grid using a pure height coordinate, with the conversion into pressure and hybrid terrain-following coordinates discussed in Appendix B.

Consider a base vertical grid, $\overline{z}$, that consists of layers at constant heights and so is uninfluenced by the terrain. The base coordinates are constructed from a set of vertical spacings between interface levels, $\Delta\overline{z}$, from a flat surface at $\overline{z} = 0$ km to the model top of $z_{\text{T}} = 20$ km. Even though we are interested in dynamics at $z = 300$ m, we require a much higher domain to successfully damp the strong hydrostatic gravity waves induced by the orography; this will be discussed further in the next subsection. A small grid spacing of $\Delta\overline{z} = 100$ m is used for the lowest levels up to 1 km, to accurately represent the orography and mesoscale dynamics. The grid is then stretched over the next 5 km to a maximum spacing of $\Delta\overline{z} = 500$ m. This resolution is retained for the remainder of the levels, as further coarsening can degrade the representation of orographic gravity waves in the sponge layer (Appendix C).

The base vertical grid is described as

$$\Delta\overline{z}_k = \begin{cases} \Delta\overline{z}_{\text{min}}, & \overline{z}_{k-0.5} \in [0, z_{\text{L}}], \\ \min\{(\Delta\overline{z}_{k-1})^{\gamma}, \Delta\overline{z}_{\text{max}}\}, & \overline{z}_{k-0.5} \in (z_{\text{L}}, z_{\text{U}}], \\ \Delta\overline{z}_{\text{max}}, & \overline{z}_{k-0.5} \in (z_{\text{U}}, z_{\text{T}}], \end{cases} \tag{9}$$

where $k \in \{1, 2, ..., N_V\}$ indexes the N_V midpoint levels, $z_{\text{L}} = 1$ km, $z_{\text{U}} = 6$ km, $z_{\text{T}} = 20$ km, $\Delta\overline{z}_{\text{min}} = 100$ m, $\Delta\overline{z}_{\text{max}} = 500$ m, and γ is a geometric stretching factor. The $N_V + 1$ interface coordinates, denoted by indices offset by 0.5, are generated as

$$\overline{z}_{k+0.5} = \overline{z}_{k-0.5} + \Delta\overline{z}_k, \tag{10}$$

https://doi.org/10.5194/egusphere-2026-2293
Preprint. Discussion started: 24 June 2026

starting from the surface at $\overline{z}_{0.5} = 0$ m. We use a stretching factor of $\gamma = 1.01679$, which means that the stretching finishes at 6007 m and the model top is 20007 m, which is very close to the 20 km target. This grid has 57 vertical levels.

2.4 Absorption of vertically propagating waves

Although our focus is on the low altitude dynamics downstream of the mountain, a large feature of these tests is strong orographic gravity waves that propagate nearly vertically. If left unimpeded, these waves will reflect off the model top and spuriously interfere with the dynamics at the lower levels. To minimise such reflections, we use a Rayleigh friction sponge layer in the upper 10 km of the domain.

For a scalar variable q, Rayleigh friction acts to damp any deviation from a reference state q_{ref} through an explicit term of

$$\frac{\partial q}{\partial t} = ... - k_R(q - q_{\text{ref}}). \tag{11}$$

The strength of the damping is given by the coefficient k_R. For a pressure-based coordinate, we choose

$$k_R = \begin{cases} \frac{1}{\tau}\sin^2\left(\frac{\pi}{2}\frac{\ln(p_c/p_k)}{\ln(p_c/p_T)}\right), & \text{if } p_k < p_c, \\ 0, & \text{else,} \end{cases} \tag{12}$$

with p_k the pressure at level k, p_c the cut-off pressure determining the onset of Rayleigh damping, $p_T = p(z_T)$ the model top pressure, and τ the damping time scale. This choice of k_R leads to a smooth increase in damping strength from the bottom of the Rayleigh friction layer to the model top. For a height-based coordinate, the coefficient can be defined as

$$k_R = \begin{cases} \frac{1}{\tau}\sin^2\left(\frac{\pi}{2}\frac{z_k - z_c}{z_T - z_c}\right), & \text{if } z_k > z_c, \\ 0, & \text{else,} \end{cases} \tag{13}$$

with z_c the height at which the Rayleigh damping layer begins.

With a 10 km thick Rayleigh friction layer ($z_c = 10$ km) and 20 km model top, $p_c \approx 305$ hPa and $p_T \approx 93$ hPa in the isothermal atmosphere. A relaxation time of $\tau = 100$ s is used, which is equivalent to $\tau_{\text{reg}} = 2000$ s on the regular-sized Earth. Further discussion of the Rayleigh damping parameters is provided in Appendix C, including showing the importance of the damping timescale (Fig. C1).

The Rayleigh friction term is discretised implicitly to ensure that the damping is unconditionally stable with regard to the timestep size. Taking a backward Euler time discretisation of (11), with superscripts denoting the time index,

$$\frac{q^{n+1} - q^n}{\Delta t} = -k_R(q^{n+1} - q_{\text{ref}}), \tag{14}$$

which can be rearranged to obtain

$$q^{n+1} = \frac{1}{1 + k_R\Delta t}q^n + \frac{k_R\Delta t}{1 + k_R\Delta t}q_{\text{ref}}. \tag{15}$$

For models that require an increment of $\Delta q = q^{n+1} - q^n$, we have

$$\Delta q = \frac{k_R\Delta t}{1 + k_R\Delta t}(q_{\text{ref}} - q^n), \tag{16}$$

https://doi.org/10.5194/egusphere-2026-2293
Preprint. Discussion started: 24 June 2026

whereas models that work with a tendency update to $\partial q/\partial t$, as in CAM, require

$$\frac{\partial q}{\partial t} \approx \frac{q^{n+1} - q^n}{\Delta t} = \frac{k_R}{1 + k_R \Delta t}(q_{\text{ref}} - q^n). \tag{17}$$

We apply Rayleigh friction to the horizontal velocities of u and v, and damp these towards a reference profile of the initial condition (1), $u_{\text{ref}} = u_0 \cos(\phi), v_{\text{ref}} = 0$. This is in contrast to typical Rayleigh damping in weather and climate models, which damps to a rest state of $u = v = 0$. Nonhydrostatic models may additionally damp the vertical velocity, but we do not include this for consistency between the hydrostatic and nonhydrostatic dynamical cores.

Dynamical cores often use Laplacian sponge layers in conjunction with, or instead of, Rayleigh damping. For consistency between models and ensuring a sufficient damping of the orographic gravity waves, we recommend switching off internal Laplacian sponge layers and adding the Rayleigh friction layer provided here, or modifying an existing sponge to the above specifications. This ensures that i) the velocities are being damped to the zonal flow reference state, ii) that a sufficiently deep damping layer is used, iii) that the damping is applied consistently between the models, including with the same timestep. This last point is crucial, as the frequency of Rayleigh damping applications varies between models: for example, MPAS applies its vertical velocity damping at every acoustic timestep (Skamarock et al., 2025), whilst Rayleigh damping on horizontal velocities in CAM-FV3 is typically used with the larger physics timestep (Harris et al., 2021). For the CAM models, we apply Rayleigh damping with the physics timestep.

3 Dynamical cores

We now briefly describe the four dynamical cores tested in DCMIP-2025. The first three models (SE, FV3, MPAS) are run through the Community Atmosphere Model (CAM) version 6. The last model is GungHo, the dynamical core used in the LFRic-Atmosphere model from the UK Met Office. Although there are nonhydrostatic versions of SE and FV3, we use the hydrostatic versions in CAM6. Both CAM-MPAS and GungHo are nonhydrostatic dynamical cores. All models are run at an approximately one-half degree horizontal resolution, which corresponds to a characteristic grid spacing of 2.25 km on the $X = 20$ small Earth.

We now briefly describe the important dynamical core choices, which are summarised in Table 2. Further description of the modelling choices can be found in the references provided, with Ullrich et al. (2017) also overviewing many of these aspects. Details about running the CAM models and the specific namelist options used in the tests are available at the GitHub repository: https://github.com/ta440/DCMIP-2025_gap_and_vortex.

3.1 CAM-SE

The spectral element model of Taylor et al. (1997) and Taylor and Fournier (2010) uses the Arakawa A-grid (Arakawa and Lamb, 1977) where variables are horizontally co-located. Each cell contains four collocation points in each dimension, corresponding to Gauss-Lobatto-Legendre nodes. An equiangular gnomonic cubed-sphere is used (Ronchi et al., 1996). A Lorenz vertical staggering is applied, where vertical velocities are computed at the interface levels and all other variables at the mid-

https://doi.org/10.5194/egusphere-2026-2293
Preprint. Discussion started: 24 June 2026

Table 2. A summary of the key model choices in the four dynamical cores.

Dynamical core	CAM-SE	CAM-FV3	CAM-MPAS	GungHo
Hydrostatic?	Hydrostatic	Hydrostatic	Nonhydrostatic	Nonhydrostatic
Spatial discretisation	Spectral Element	Finite volume	Finite volume	Compatible finite element
Horizontal grid	Equiangular gnomonic cubed-sphere	Equi-edge gnomonic cubed-sphere	Centroidal Voronoi	Equiangular gnomonic cubed-sphere
Vertical coordinate	Hybrid pressure, floating Lagrangian	Hybrid pressure, floating Lagrangian	Hybrid z, fixed in time	Hybrid z, fixed in time
Horizontal staggering	A-grid	CD-grid	C-grid	C-grid
Vertical staggering	Lorenz	Lorenz	Lorenz	Charney-Phillips
Temporal discretisation	5-stage RK3	Forward-backward	Split-explicit	Semi-implicit quasi-Newton

point levels. The floating Lagrangian level method of Lin (2004) is used, which removes the explicit computation of vertical transport, along with the hybrid pressure coordinate of Simmons and Burridge (1981) in dry simulations. The time discretisation is the five-stage, third-order, Runge-Kutta scheme of Kinnmark and Gray (1984), described in Guerra and Ullrich (2016). Diffusion is primarily implemented through fourth-order hyperdiffusion, with a stronger coefficient applied to divergent components of the horizontal flow compared to rotational motions. We use the hydrostatic version of SE available in CAM, but nonhydrostatic SE versions exist in other code bases such as HOMME (Taylor et al., 2020). A description of integrating the SE dynamical core into CAM can be found in Lauritzen et al. (2018). The one-half degree configuration is called ne60, which specifies that the cubed-sphere panels have 60 elements along each edge. SE is a compatible model, also termed mimetic, which means that discrete analogues of the vector calculus identities curl(grad) = div(curl) = 0 are preserved (Taylor and Fournier, 2010).

3.2 CAM-FV3

FV3 is a finite-volume cubed-sphere model from NOAA GFDL (Harris et al., 2021). At its heart is the finite-volume transport scheme of Lin and Rood (1996) which uses the piecewise parabolic method (PPM) for subgrid reconstructions (Colella and Woodward, 1984). FV3 uses floating Lagrangian levels (Lin, 2004), a hybrid pressure coordinate, and a Lorenz vertical staggering. We run CAM-FV3 with its default horizontal transport scheme, which is monotonic with Huynh (2007) constraints applied in certain circumstances; this option is more diffusive than the unlimited methods available, but is more stable. FV3

https://doi.org/10.5194/egusphere-2026-2293
Preprint. Discussion started: 24 June 2026

uses a unique equi-edge variant of the gnomonic cubed-sphere grid (Chen, 2021) that leads to more uniform cells at panel edges compared to the equiangular mapping, as further discussed by Santos (2024) and Andrews and Jablonowski (2025). The cubed-sphere panel edges are located at $\lambda \in \{35°, 125°, 215°, 305°\}$, which is a 10-degree westward shift from the positions used in CAM-SE and GungHo. FV3 primarily uses the D-grid to store the prognostic variables, but uses interpolated C-grid winds for the transport scheme; this approach is referred to as the CD-grid, although its representation of waves is very similar to that of the D-grid (Skamarock, 2008; Konor and Randall, 2018). FV3's main explicit diffusion mechanism is hyperdiffusive divergence damping (sixth-order is used in this paper), along with implicit diffusion of vorticity through the transport scheme, although a range of other diffusion mechanisms are available (Harris et al., 2021). Explicit forward Euler timestepping is used for the hydrostatic model.

3.3 CAM-MPAS

The Model for Prediction Across Scales (MPAS) (Skamarock et al., 2012, 2025) uses an Arakawa C-grid staggering on a centroidal Voronoi mesh (Ju et al., 2011), with the TRiSK modification of Thuburn et al. (2009) and Ringler et al. (2010) for an accurate representation of the Coriolis force. Whilst the centroidal Voronoi mesh primarily contains hexagonal cells, there are also some pentagons and heptagons. Additionally, the centroidal Voronoi mesh is not symmetrical with respect to the equator, unlike a gnomonic cubed-sphere grid. MPAS uses a finite volume spatial discretisation of the nonhydrostatic equations. The prognostic variables are in a flux form that includes the density of dry air, e.g. ρu, which naturally ensures that the scalar transport equations are conservative. MPAS uses a Lorenz vertical staggering and a hybrid z-coordinate that blends pure height and terrain-following coordinates, with additional smoothing for steeper orography (Klemp, 2011). Dissipation in MPAS includes second-order fixed or Smagorinsky diffusion, fourth-order hyperviscosity, and a three-dimensional divergence damping of acoustic waves (Skamarock and Klemp, 1992). The time discretisation uses a split-explicit approach with smaller timesteps for the acoustic modes (Wicker and Skamarock, 2002).

3.4 GungHo

The GungHo dynamical core (Melvin et al., 2019, 2024) uses a compatible finite element discretisation. The specific choice of compatible function spaces mimics the C-grid staggering and ensures properties such as mass conservation and the preservation of steady geostrophic modes (Cotter and Shipton, 2012). The chosen function spaces also mimic the Charney-Phillips vertical staggering, where thermodynamic variables such as the potential temperature are co-located with the vertical velocity at layer interfaces, so are offset from the horizontal velocities and other scalar variables. An equiangular cubed-sphere grid and a hybrid z-coordinate are used. Timestepping is performed with the semi-implicit quasi-Newton (SIQN) method (Hartney et al., 2025; Wood et al., 2014), where an inner loop solves fast terms implicitly, and an outer loop computes the transport and slower terms explicitly. Two inner and two outer loops are typically used. GungHo does not require explicit diffusion for stability due to its use of compatible function spaces, although there are still sources of implicit diffusion, such as from off-centring in the SIQN inner loop and limiters in the flux-form semi-Lagrangian transport scheme (Bendall and Kent, 2025).

https://doi.org/10.5194/egusphere-2026-2293
Preprint. Discussion started: 24 June 2026

Dynamical core	CAM-SE	CAM-FV3	CAM-MPAS
Lagrangian remapping subcycles	2 (`n_split`)	2 (`k_split`)	N/A
Tracer transport subcycles	1 (`q_split`)	N/A	2 (`number_of_sub_steps`)
Dynamics subcycles	3 (`r_split`)	6 (`n_split`)	3 (`dynamics_split_steps`)
Hyperviscosity subcycles	3 (`hypervis_subcycle`)	N/A	N/A

Table 3. Comparing the default subcycling parameters for the CAM dynamical cores. For a physics timestep of 45 s in our tests, the dynamics timesteps are 7.5 s for CAM-SE, 3.75 s for CAM-FV3, and 7.5 s for CAM-MPAS. Note that CAM-SE by default applies hyperviscosity subcycling, which means the explicit diffusion is applied on a smaller timestep of 2.5 s.

An additional distinction of GungHo is that it is a deep atmosphere model, whereas the CAM dynamical cores assume a shallow atmosphere. This means that GungHo does not make either the traditional approximation, which removes the non-traditional Coriolis and metric terms, or the shallow fluid approximation, where the Earth's radius of a is used instead of the actual vertical location of $a + z$ in the governing equations (see Chapter 2.2.4 of Vallis (2017)). Tests in GungHo where the nontraditional Coriolis terms were removed had minimal impact, showing that the use of the deep atmosphere is not an important factor in these tests. However, we note that the use of a deep atmosphere could lead to significant differences in other test cases, specifically those on a small Earth, as the X factor increases vertical velocities, and will thus scale up the strength of the nontraditional $2\Omega w \cos(\phi)$ term.

3.5 Timestep sizes

A variety of timesteps are used in dynamical cores for different components according to characteristic timescales. Physics terms typically use the largest timestep, which is then divided by an integer for the tracer transport timestep. Some models then apply further subcycling to have a smaller dynamics timestep to stably handle the rapidly propagating acoustic waves. Another potentially different timestep size is for remapping the vertical Lagrangian levels back to undeformed reference levels in CAM-SE and CAM-FV3. CAM-SE also performs subcycling of the hyperviscosity terms within each dynamics timestep, and this is typically required for stability due to a strong diffusion of the divergent motions (Lauritzen et al., 2018). A comparison of the temporal subcycling parameters in the CAM dynamical cores is shown in Table 3.

The same physics timestep of $\Delta t_{\text{phys}} = 45$ s is used in this test case for all the dynamical cores. This is a factor of $X = 20$ reduction from the default timestep of $\Delta t_{\text{phys}} = 900$ s for CAM-SE and CAM-FV3 at a one-half degree resolution. Although these tests do not include physics, the physics timestep is used for the Rayleigh damping terms (Sect. 2.4). The corresponding dynamics timesteps in the CAM dynamical cores are 7.5 s for CAM-SE, 3.75 s for CAM-FV3, and 7.5 s for CAM-MPAS. The physics timestep is used for each SIQN timestep in GungHo, as its inner loop linear solver allows stability with much larger timesteps than explicit methods.

https://doi.org/10.5194/egusphere-2026-2293
Preprint. Discussion started: 24 June 2026

3.6 Post-processing

For a fair comparison between models, simulation outputs are interpolated from the model's native grid to a regular $0.5° \times 0.5°$ lon-lat grid, with 720 longitude points and 361 latitude points. Visualisations of each case are made at a fixed height of 300 m, using a cubic interpolation of information from the lowest four model levels. Geopotential heights in CAM are accessed through the `Z3` diagnostic field. For the figures in the following sections, we shade the orography at 300 m in grey.

4 Case A: Gap flow

We now describe the first variant of orography in this test case, which simulates flow through a gap in a mountain chain.

4.1 Specifications

The surface height is defined using exponential functions, similarly to the orography of Hughes and Jablonowski (2023). The functional form of the mountain chain is

$$f(\lambda,\phi) = h_0 \exp\left(-\left(\frac{\lambda-\lambda_\mathrm{c}}{d_1}\right)^{e_1} - \left(\frac{\phi-\phi_\mathrm{c}}{d_2}\right)^{e_2}\right), \tag{18}$$

and the gap is

$$g(\lambda,\phi) = 1 - \exp\left(-\left(\frac{\phi-\phi_\mathrm{c}}{d_3}\right)^{e_3}\right), \tag{19}$$

where $(\lambda_\mathrm{c},\phi_\mathrm{c}) = (\pi, 0)$ specifies the centroid of the mountain chain orography and the middle point of the gap, e_i are shape exponents, and d_i are length factors. The orography is constructed as $z_\mathrm{s}(\lambda,\phi) = f(\lambda,\phi)g(\lambda,\phi)$, with $g(\lambda,\phi)$ removing a section of the mountain chain to create the gap. The longitudinal position of the orography is arbitrary, but locating it at the centre of the domain with $\lambda \in [0, 2\pi)$ simplifies the computation of the great circle distance. The mountain height is $h_0 = 1500$ m.

We define the orography through length scales for the longitudinal extent (x_lon), latitudinal extent (x_lat), and gap extent (x_gap). These scales define the span of the highest 90 % of the orography, or equivalently, twice the distance from the centroid to where the orography drops below 10 % of the maximum height ($z_\mathrm{s}/h_0 < 0.1$). On the small Earth, the longitude and latitude length scales are $x_\mathrm{lon} = X^{-1} \cdot 800$ km $= 40$ km and $x_\mathrm{lat} = X^{-1} \cdot 6000$ km $= 300$ km, respectively, and the gap width is $x_\mathrm{gap} = X^{-1} \cdot 1000$ km $= 50$ km. Cross-sections of the orography in Figure 2 show that this gap width is sufficiently well resolved at an approximately one-half degree horizontal resolution, with at least three points on the slopes.

We choose shape exponents of $e_1 = e_2 = e_3 = 10$. The length factors for the mountain chain (18) and gap (19) are computed as

$$d_i = \frac{x_i}{2a} \ln\left(\frac{h_0}{z_\mathrm{s}}\right)^{-1/e_i}, \tag{20}$$

for $i \in \{1, 2, 3\}$ and $x_1 = x_\mathrm{lon},\ x_2 = x_\mathrm{lat},\ x_3 = x_\mathrm{gap}$, with a the radius of the small Earth (Table 1) and $h_0/z_\mathrm{s} = 10$.

We compute the hydrostaticity number (7) using a characteristic length scale of the longitudinal mountain extent, $L_\mathrm{h} = x_\mathrm{lon}$. Using the maximum zonal wind speed for the characteristic velocity ($U = 10$ m s^{-1}), the hydrostaticity number is Hy $= 11.6$.

https://doi.org/10.5194/egusphere-2026-2293
Preprint. Discussion started: 24 June 2026

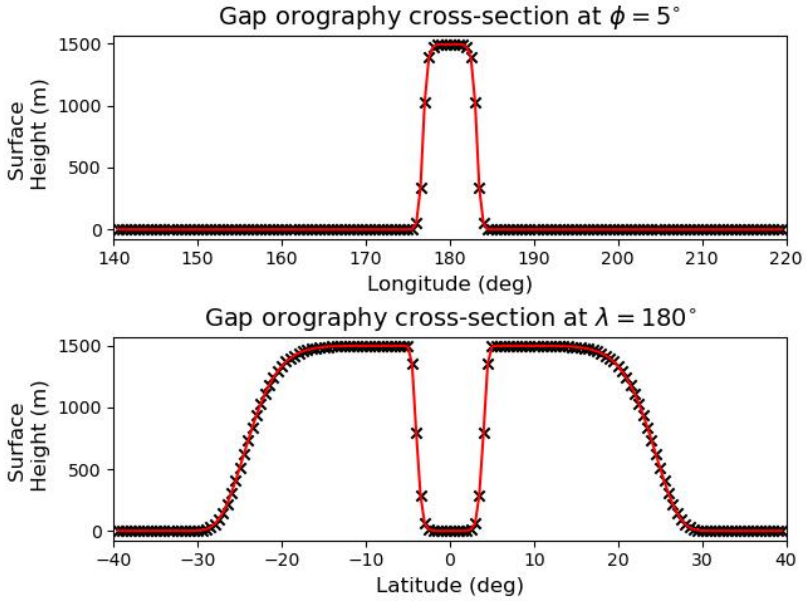

Figure 2. Cross-sections of the mountain chain in the gap flow test, showing the surface height of $z_s = \Phi_s/g$. The black crosses indicate grid points at the half-degree horizontal resolution in CAM-SE. The fixed latitude cross-section uses $\phi = 5^\circ$ to show the mountain orography instead of the gap. The cross-sections show that the steep slopes of the mountain chain and the gap are sufficiently resolved at this horizontal resolution.

As Hy $>> 1$, the gravity waves excited by the mountain chain are highly hydrostatic and propagate nearly directly vertically. An inverse Froude number (4) of $\mathrm{Fr}^{-1} = 2.73$ means that the gap flow is in the nonlinear regime.

4.2 Test case dynamics

We now describe the dynamics of the gap flow test in a simulation for 0.5 days (10 days on the small Earth). We examine fields of the normalised zonal wind perturbation,

$$u'(\lambda, \phi) = \frac{u(\lambda, \phi) - u_0 \cos(\phi)}{u_0 \cos(\phi)}, \tag{21}$$

and temperature perturbation,

$$T'(\lambda, \phi) = T(\lambda, \phi) - T_0, \tag{22}$$

at a height of $z = 300$ m. A normalised zonal wind perturbation of $u' > 0$ represents flow acceleration and $u' < 0$ is deceleration, with $u' < -1$ meaning the flow has reversed direction and become an easterly wind. Field extrema are computed away from the mountain, $\lambda \notin [170^\circ, 190^\circ]$, which avoids any spurious values from interpolation around the orography.

Figures 3 and 4 show the evolution of the u' and T' fields, using simulations with the CAM-SE dynamical core. For both the with and without rotation configurations, there are accelerated winds through the gap as seen in the zonal wind perturbation

https://doi.org/10.5194/egusphere-2026-2293
Preprint. Discussion started: 24 June 2026

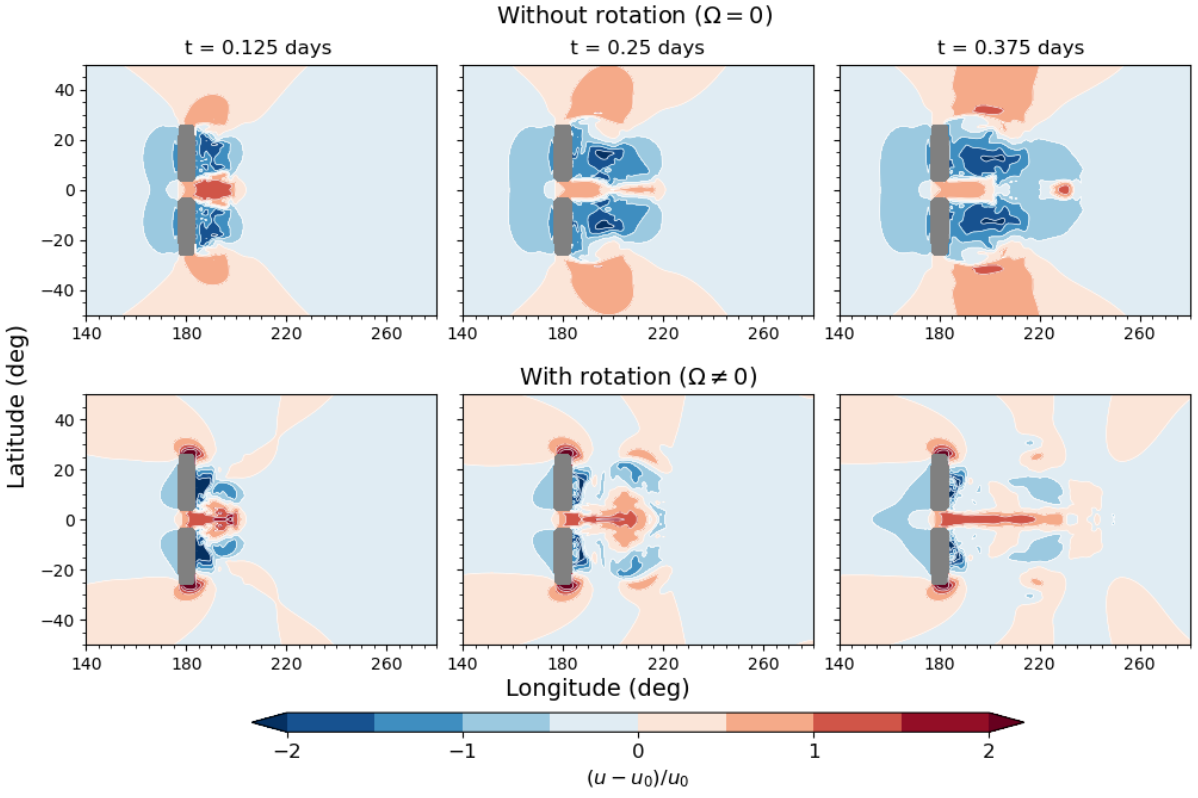

Figure 3. Comparing the normalised zonal wind perturbation, u', at selected times during the gap flow test, without rotation (top row) and with rotation (bottom row), and plotted at $z = 300$ m. These plots show CAM-SE simulations.

field (Fig. 3), with westerly wind speeds in excess of 20 m s^{-1} ($u' > 1$). In the case without rotation, the frontmost part of the accelerated flow detaches and travels downstream, as seen at $t = 0.25$ days and $t = 0.375$ days. This does not occur in the case with rotation, with the stream of accelerated flow instead expanding as a single jet along the equator. In both cases, there are regions of decelerated ($u' < 0$) and even reversed ($u' < -1$) flow on both sides of the mountain chain, with small regions where the easterly winds are larger than 10 m s^{-1} ($u' < -2$). In the case without the Coriolis force, the region of reverse flow grows over time in its longitudinal extent, whilst with rotation, the region of reversed flow attached to the mountain is smaller and relatively static during the simulation.

Visualisations of the temperature perturbation (Fig. 4) highlight the formation of lee vortices that detach from the mountain orography in this nonlinear flow-around regime. In the case without rotation, these vortices form around the edges of the mountain chain and propagate eastwards at a relatively constant latitude. This response is similar to simulations for bell-shaped mountains in Smolarkiewicz and Rotunno (1989) and for a mountain chain orography in Epifanio and Durran (2002). With rotation, the detached vortices instead form around the edges of the gap, and these propagate both zonally and meridionally, as they are transported polewards during the simulation.

https://doi.org/10.5194/egusphere-2026-2293
Preprint. Discussion started: 24 June 2026

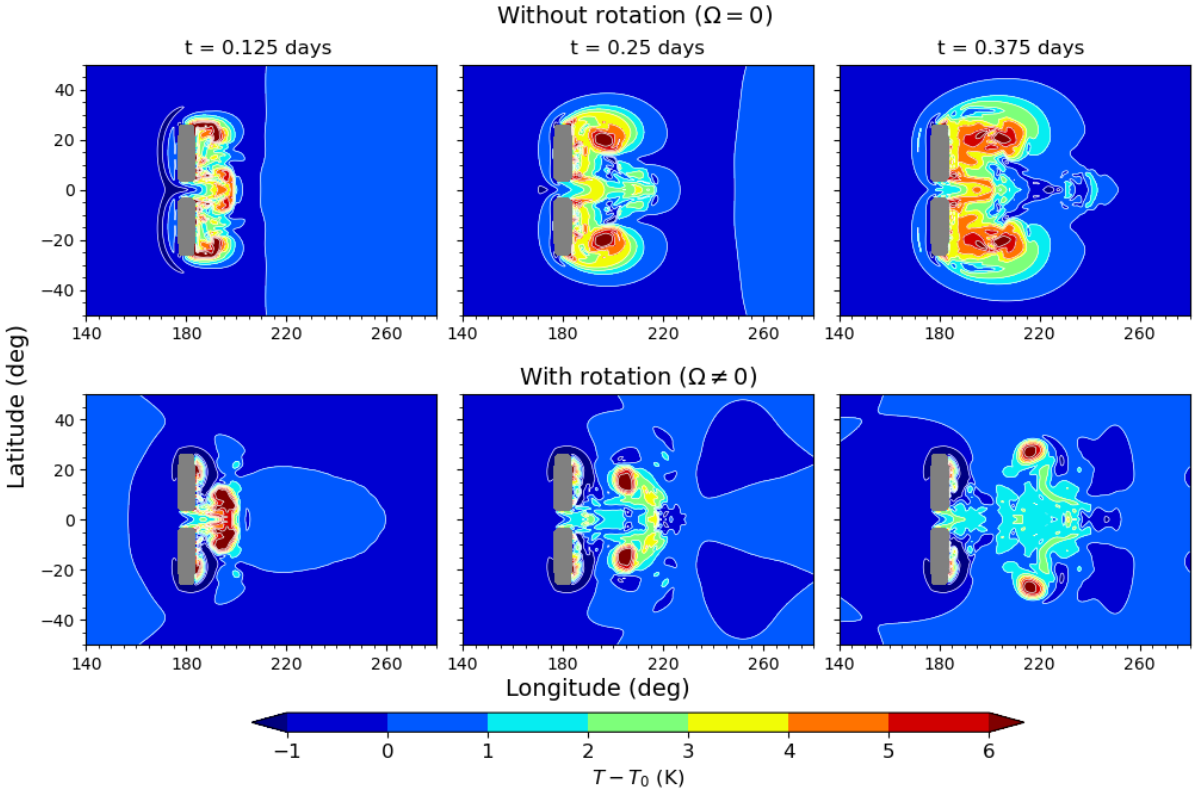

Figure 4. Comparing the temperature perturbation, T', at selected times during the gap flow test, without rotation (top row) and with rotation (bottom row), and plotted at $z = 300$ m. These plots show CAM-SE simulations.

4.3 Dynamical core comparisons

Comparisons of the dynamical core simulations after 0.5 days are shown in Figures 5 and 6 for the case without rotation. All dynamical cores replicate the large-scale dynamics of accelerated flow through the gap ($u' > 0$) and regions of reversed flow ($u' < -1$) (Fig. 5). The detached region of accelerated flow is also observed in all the dynamical cores, although it is asymmetrical in CAM-MPAS and has a higher amplitude in GungHo. The fields in CAM-SE are the smoothest, as is clearly seen in the temperature perturbation (Fig. 6), and this is likely a result of its strong hyperdiffusion acting on the divergent motions; this is examined further in Sect. 6.1. By contrast, the fields from CAM-FV3 and GungHo contain more small-scale features. Due to the irregular Voronoi mesh, CAM-MPAS has fields that are asymmetric about the equator. The other three models, which use cubed-sphere grids, have fairly symmetrical fields. Any small asymmetries in GungHo may have been introduced through the SIQN timestepper, with an asymmetrical looping over columns for the global summations in the linear solver (Maynard et al., 2020).

https://doi.org/10.5194/egusphere-2026-2293
Preprint. Discussion started: 24 June 2026

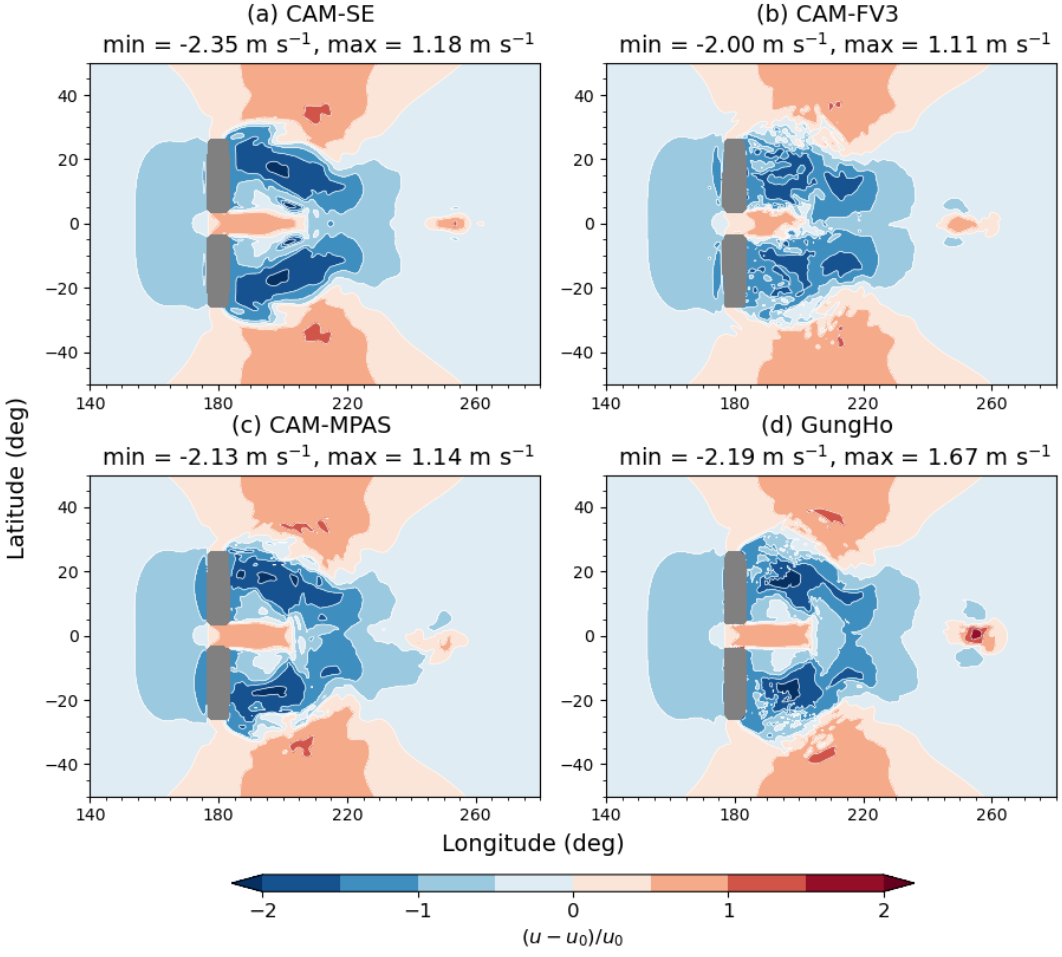

Figure 5. Normalised zonal wind perturbation, u', at the end of the gap flow test (0.5 days) *without* rotation, plotted at $z = 300$ m.

Figures 7 and 8 compare gap flow simulations with rotation. CAM-SE and CAM-MPAS have the smoothest jets of accelerated flow along the equator (Fig. 7), whilst those from CAM-FV3 and GungHo are patchier. The shape of the reversed flow to the west of the orography is also different in GungHo compared to the CAM dynamical cores. The profiles of the lee vortices in the $T^{'}$ field (Fig. 8) are similar for CAM-SE and CAM-MPAS. By comparison, the vortices in GungHo and CAM-FV3 are more elliptical and are also transported by a slightly smaller amount.

https://doi.org/10.5194/egusphere-2026-2293
Preprint. Discussion started: 24 June 2026

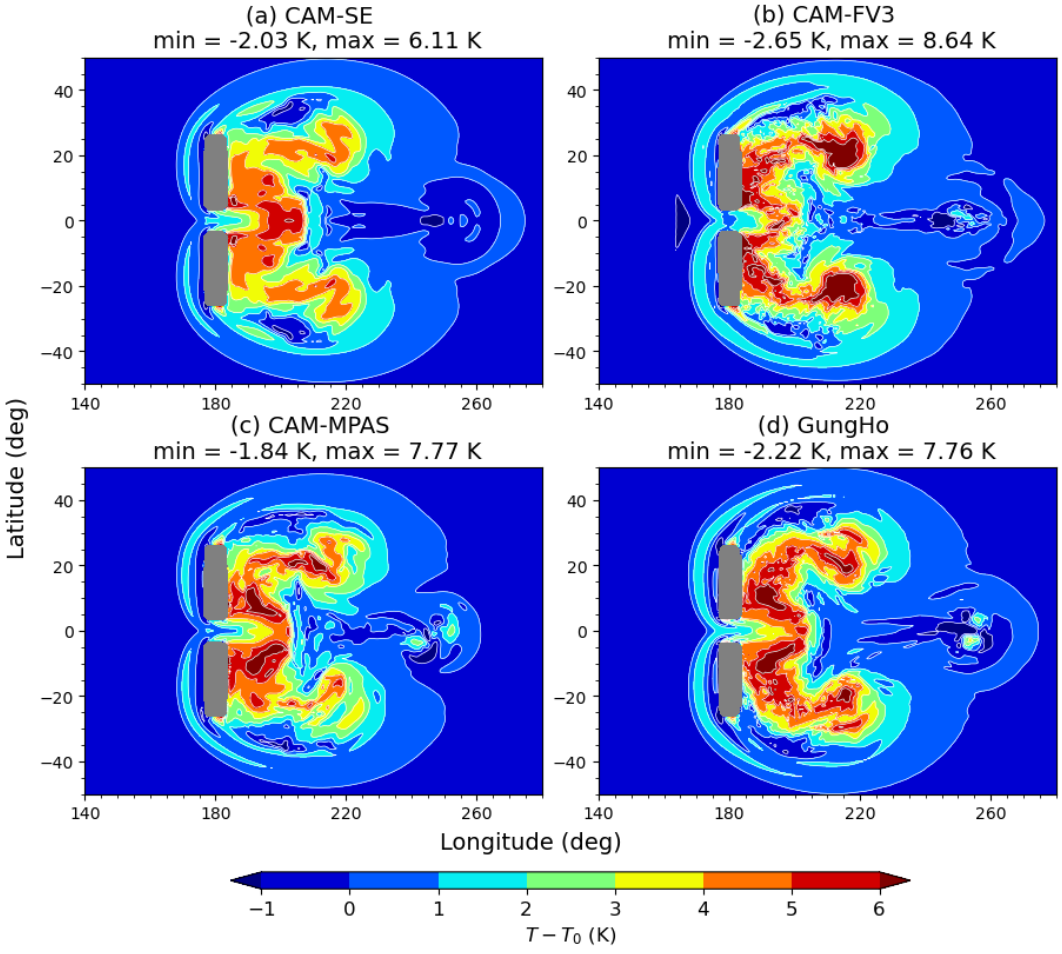

Figure 6. Temperature perturbation, T', at the end of the gap flow test (0.5 days) *without* rotation, plotted at $z = 300$ m.

https://doi.org/10.5194/egusphere-2026-2293
Preprint. Discussion started: 24 June 2026

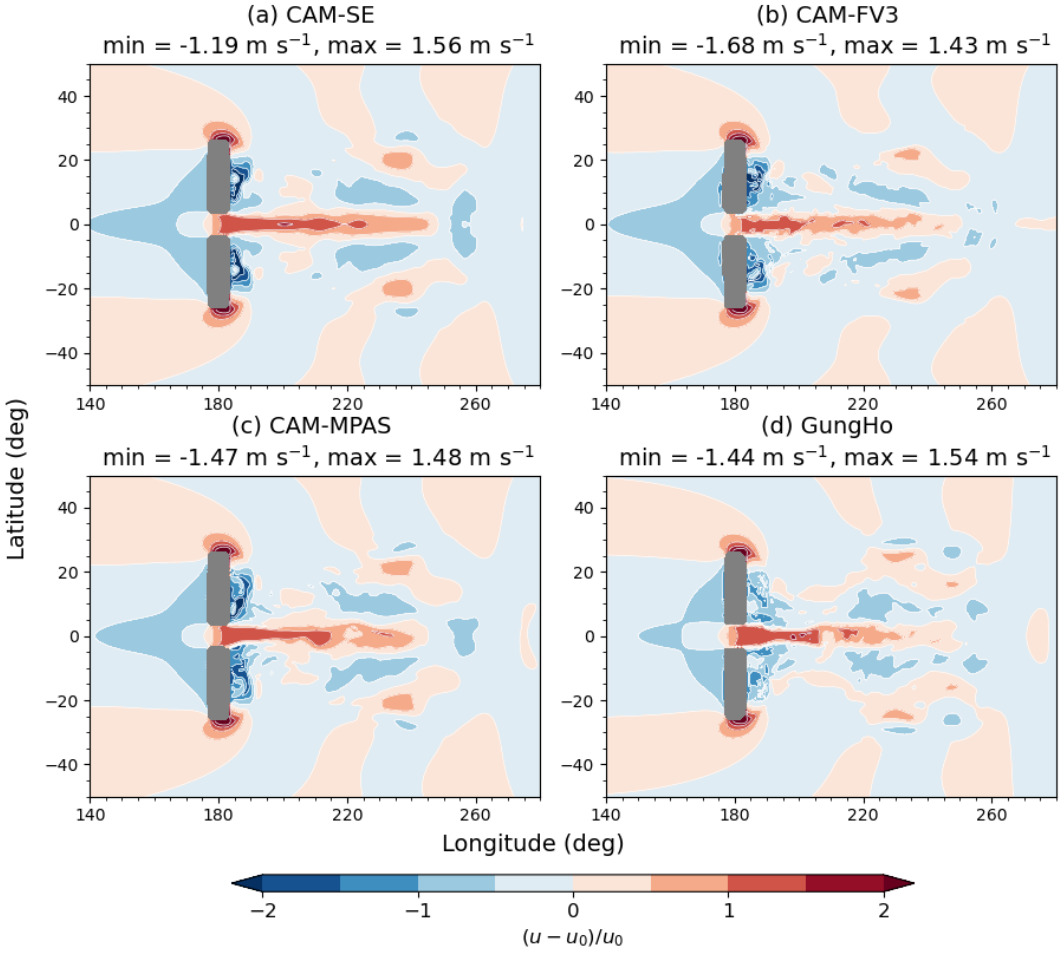

Figure 7. Normalised zonal wind perturbation, u', at the end of the gap flow test (0.5 days) *with* rotation, plotted at $z = 300$ m.

https://doi.org/10.5194/egusphere-2026-2293
Preprint. Discussion started: 24 June 2026

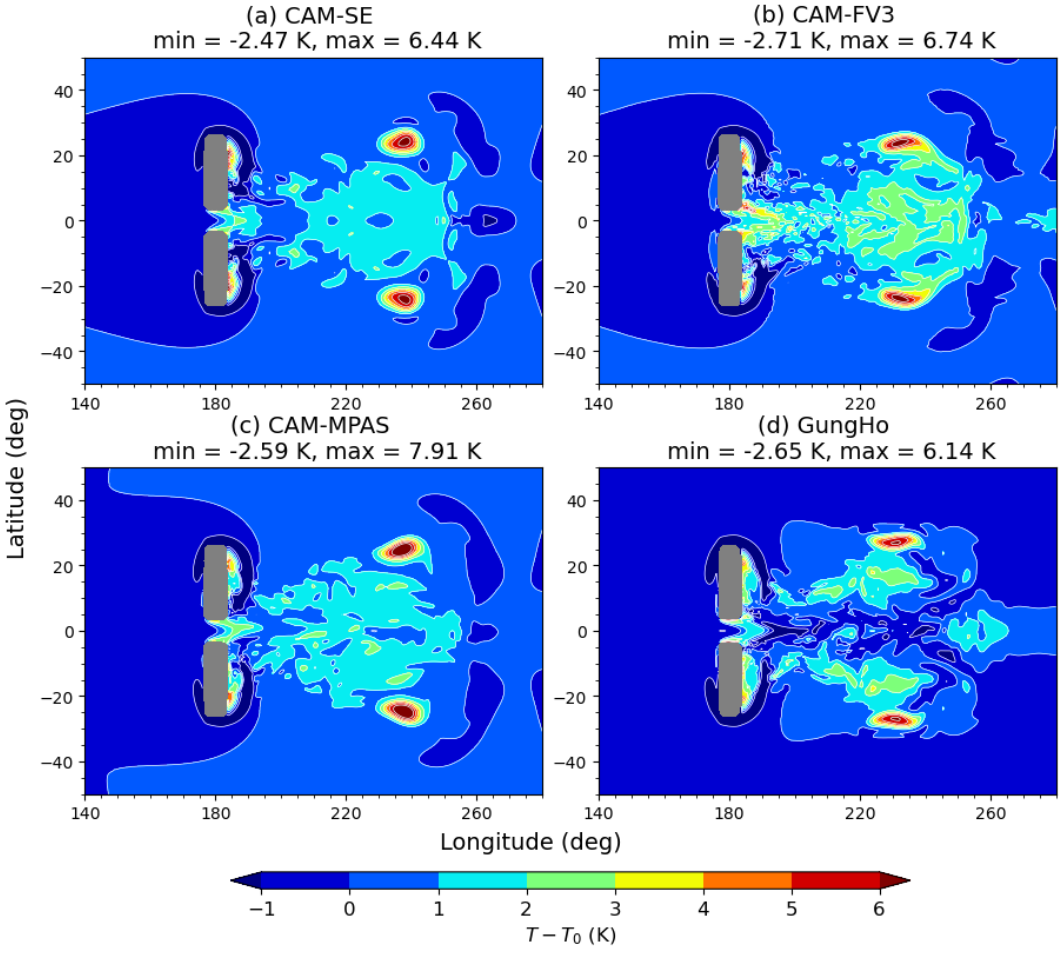

Figure 8. Temperature perturbation, T', at the end of the gap flow test (0.5 days) *with* rotation, plotted at $z = 300$ m.

https://doi.org/10.5194/egusphere-2026-2293
Preprint. Discussion started: 24 June 2026

5 Case B: Vortex shedding

We now move to the second orography variant, where an isolated mountain generates the shedding of vortices downstream.

5.1 Specifications

The orography is inspired by the approximately circular island of Gran Canaria, off the coast of Northwestern Africa. We model this with a Gaussian function of

$$z_\mathrm{s}(\lambda,\phi) = h_0 \exp\left(-\left(\frac{r}{d}\right)^2\right), \tag{23}$$

where r is the great circle distance,

$$r = a\arccos(\sin(\phi)\sin(\phi_\mathrm{c}) + \cos(\phi)\cos(\phi_\mathrm{c})\cos(\lambda-\lambda_\mathrm{c})). \tag{24}$$

The Gaussian half-width is set to $d = X^{-1}\cdot 250$ km $= 12.5$ km on the $X = 20$ small Earth, meaning that four half-widths are equal to the approximate 50 km diameter of Gran Canaria. A mountain height of $h_0 = 2000$ m replicates Gran Canaria's approximate height-to-diameter ratio of 0.04.

The mountain is centred at $(\lambda_\mathrm{c},\phi_\mathrm{c}) = (\pi,\pi/9)$. Whilst the longitudinal position of the orography is arbitrary in this test, the latitudinal position is key to the vortex shedding dynamics. A mountain centred at the equator would only lead to the shedding of a pair of lee vortices, like in the gap flow test (Figure 4). Any offset from the equator leads to an asymmetry in the flow field, due to the initial zonal flow of $u_0\cos(\phi)$ that decays towards the poles. Flow asymmetry is crucial to generating vortex shedding; previous studies instead used an asymmetrical temperature perturbation (Schär and Durran, 1997) or a velocity perturbation and asymmetrical orography (Sun and Chern, 1994) to instigate atmospheric vortex streets.

Following Sun and Chern (1994), we investigate the vortex shedding at a height of 300 m. The cross-sectional diameter of the mountain at this altitude is approximately $2.75d = 34.4$ km, which covers about six degrees on the small Earth. The initial velocities over the northern and southern slopes at $z = 300$ m are $u(\phi = 23°, t = 0) = 9.21$ m s^{-1} and $u(\phi = 17°, t = 0) = 9.56$ m s^{-1}, respectively, with this velocity differential instigating the asymmetrical vortex shedding.

We compute nondimensional numbers at the mountain centroid and use a characteristic velocity of $U = u(\phi = 20°, t = 0) = 9.40$ m s^{-1}. We assume that one Gaussian half-width corresponds to one-quarter of a characteristic terrain wavelength, thus $L_\mathrm{h} = 4d$. This leads to a hydrostaticity number (7) of $\mathrm{Hy} = 15.4$ and an inverse Froude number (4) of $\mathrm{Fr}^{-1} = 3.87$. Hence, like with the gap flow case, the orographic gravity waves are highly hydrostatic and the mesoscale flow is nonlinear. The flow satisfies $\mathrm{Fr}^{-1} > 2.5$, which Etling (1989) gives as a requirement for atmospheric vortex streets.

An important nondimensional number for vortex shedding is the Strouhal number,

$$\mathrm{St} = \frac{L_I}{UT_\mathrm{S}}, \tag{25}$$

where L_I is a length scale of the object impeding the flow, with $L_I = 2.75d$ at our altitude of interest ($z = 300$ m), and U is a characteristic velocity. T_S is the time period between the shedding of two vortices with the same sign of relative vorticity,

https://doi.org/10.5194/egusphere-2026-2293
Preprint. Discussion started: 24 June 2026

with positive ζ being cyclonic vortices that rotate anticlockwise in the Northern hemisphere, and negative ζ being anticyclonic vortices that rotate clockwise. There is noted variation in Strouhal numbers for atmospheric vortex streets, with observational examples of 0.14–0.16 for Maderia in Gao et al. (2023), 0.09–0.12 for Guadalaupe in Horváth et al. (2020), 0.13–0.28 for the Tibetan plateau in Liu et al. (2023), and 0.15–0.22 in the numerical studies of Nunalee and Basu (2014) for quasi-idealised terrain over a range of characteristic length scales. We will soon compare estimated Strouhal numbers in our test case to these values from the literature.

It is important to note that vortex shedding is a complex phenomenon that is also dependent on the viscosity of the flow, typically measured through the Reynolds number. In a dynamical core, the effective combined strength of the explicit and implicit numerical diffusion will thus impact the flow regime of the vortex shedding. This plays into the model differences observed in this test case.

5.2 Test case dynamics

For the vortex shedding case, we again show the normalised zonal wind perturbation of u' (21), but this time along with the relative vorticity in the horizontal dimension,

$$\zeta = \frac{1}{a\cos(\phi)}\left(\frac{\partial v}{\partial \lambda} - \frac{\partial}{\partial \phi}(u\cos(\phi))\right). \tag{26}$$

We compute relative vorticities using the Python package `metpy` (May et al., 2022) then multiply the result by $X = 20$ to account for the reduced radius (a) of the small Earth. When plotting the relative vorticity, the colorbar is saturated to highlight the vortices. Field extrema are computed away from the mountain, $\lambda \notin [175°, 185°]$, which avoids spurious values from interpolation around the orography. The simulation time is one day (20 small Earth days), so twice the length of the gap flow test.

Snapshots during CAM-FV3 simulations in Figures 9 and 10 show that vortex shedding is instigated both in the presence and absence of the Coriolis force. Without rotation, an oscillatory pattern of decelerated flow ($u^{'} < 0$) forms downstream of the mountain as the vortices are shed, with localised accelerations on the outside of this pattern (Fig. 9). There is a clear vortex street constructed at a constant shedding frequency, and this is best seen in the relative vorticity field (Fig. 10). Five pairs of vortices are generated over the one-day simulation, so the shedding frequency is $T_S \approx 4.8$ hours. The corresponding Strouhal number (25) is St ≈ 0.21, which is within the observed and modelled range for atmospheric vortex streets. An oscillatory pattern of decelerated flow ($u^{'} < 0$) forms downstream of the mountain as the vortices are shed, with localised accelerations on the outside of this pattern (Fig. 9). The magnitudes of the cyclonic and anticyclonic vortices are similar.

In the test with rotation, the shedding generates dominant cyclonic vortices. The leading cyclonic vortex is transported polewards, which contrasts with the more confined zonal propagation in the $\Omega = 0$ s^{-1} case. The flow disturbances travel further in the simulation with the Coriolis force. The frequency of the vortex shedding is also faster, with nine shed cyclonic vortices, so $T_S \approx 2.7$ hours and St ≈ 0.38. Whilst this Strouhal number is larger than those in the literature, this may be due to the scaled Coriolis force on the small Earth.

https://doi.org/10.5194/egusphere-2026-2293
Preprint. Discussion started: 24 June 2026

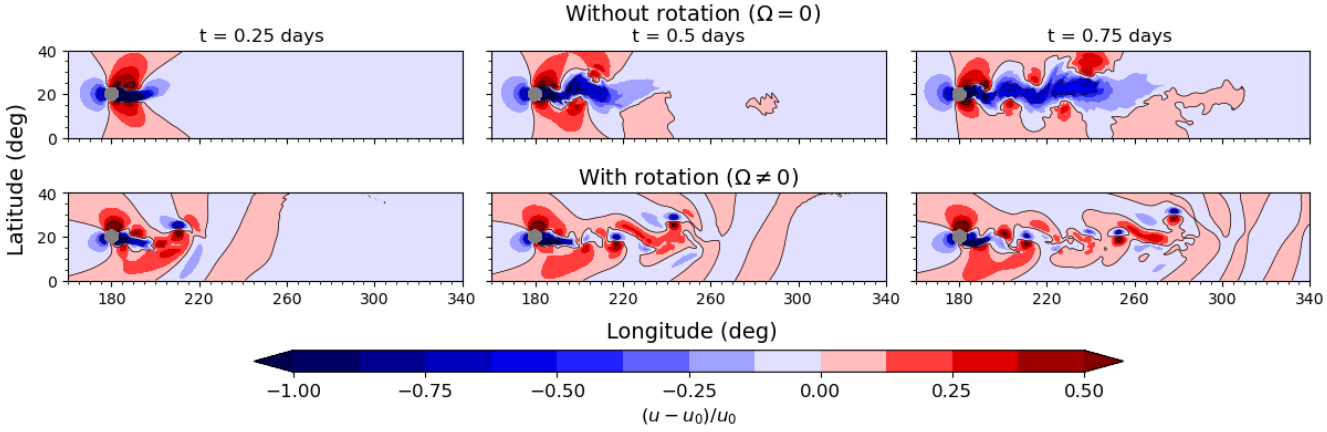

Figure 9. Zonal wind perturbation, u', at selected times during the vortex shedding test, with and without rotation, and plotted at $z = 300$ m. These plots show CAM-FV3 simulations.

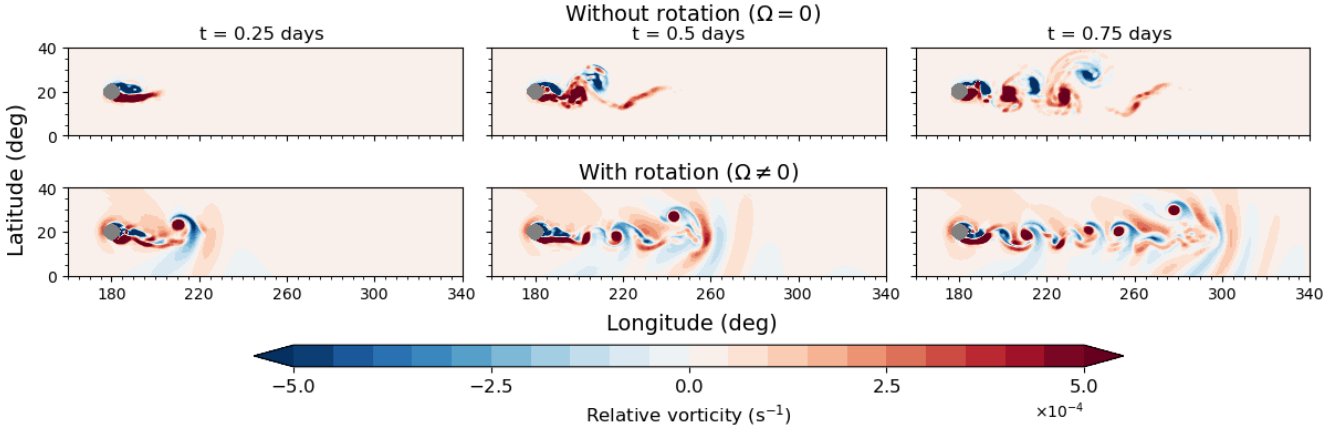

Figure 10. Relative vorticity, ζ, at selected times during the vortex shedding test, with and without rotation, and plotted at $z = 300$ m. These plots show CAM-FV3 simulations.

https://doi.org/10.5194/egusphere-2026-2293
Preprint. Discussion started: 24 June 2026

5.3 Dynamical core comparisons

In the case without rotation, the oscillatory patterns of decelerated flow differ between dynamical core (Fig. 11). CAM-FV3 has the clearest oscillations in latitude, which is also reflected in the most regular vortices (Fig. 12). This may be due to its primary use of the D-grid, which often allows for a more accurate representation of vorticity dynamics than the C-grid (Harris et al., 2021). The final locations of the shed vortices also differ between the dynamical cores (Fig. 12). CAM-FV3 has the tightest latitudinal range of the vortices, while CAM-MPAS has a street that curves towards the equator. It is likely that model-specific diffusion plays a large role in these variations. GungHo, which applies no explicit diffusion, has more grid-scale noise in the output fields. CAM-SE has the smallest vorticity magnitudes, with its strong hyperdiffusion. The leading vortex in CAM-FV3 is also highly diffused, whereas it is more preserved in the other three models.

In the case with rotation, the vortex shedding frequencies are again roughly the same in each model. Whilst the flow fields from each model have similar features, with diagonal bands of accelerated flow, each field has significant variation (Fig. 13). This is also observed through the relative vorticity (Fig. 14), with differences between the locations and magnitudes of the dominant cyclonic vortices. In all models, the leading cyclonic vortex is quite well maintained after one day, whilst the second cyclonic vortex is highly diffused. As in the case without rotation, the maximum vorticity magnitude is smallest in CAM-SE, and CAM-FV3 and GungHo show the least diffused fields.

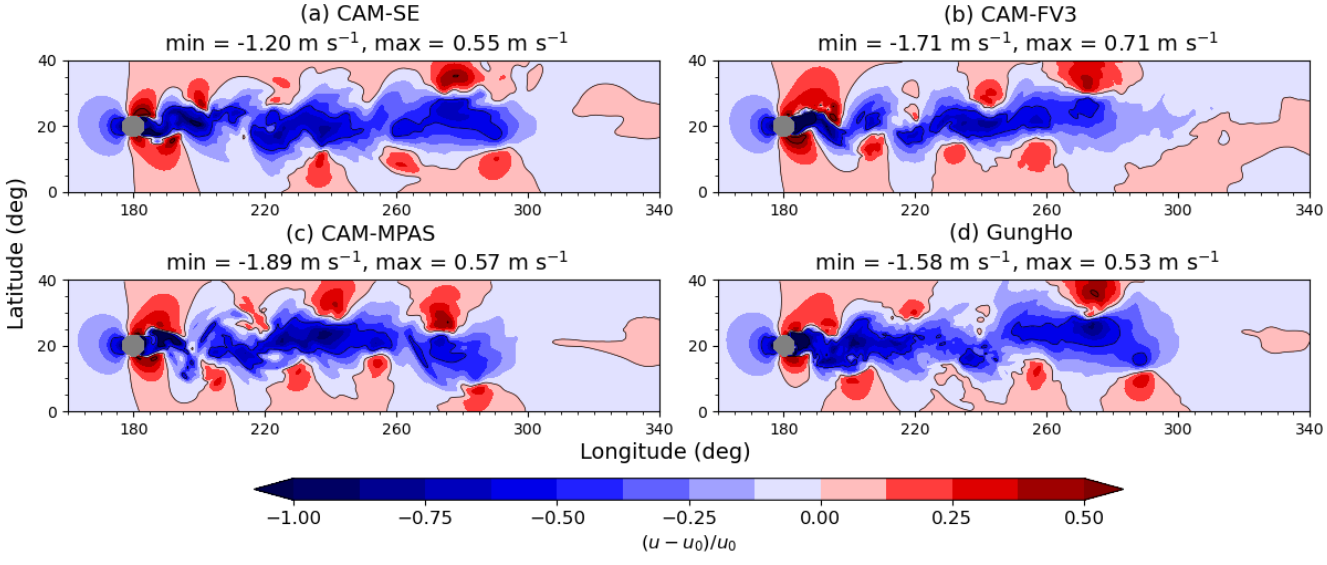

Figure 11. Normalised zonal wind perturbation, u', at the end of the vortex shedding test (1 day) *without* rotation, plotted at $z = 300$ m.

https://doi.org/10.5194/egusphere-2026-2293
Preprint. Discussion started: 24 June 2026

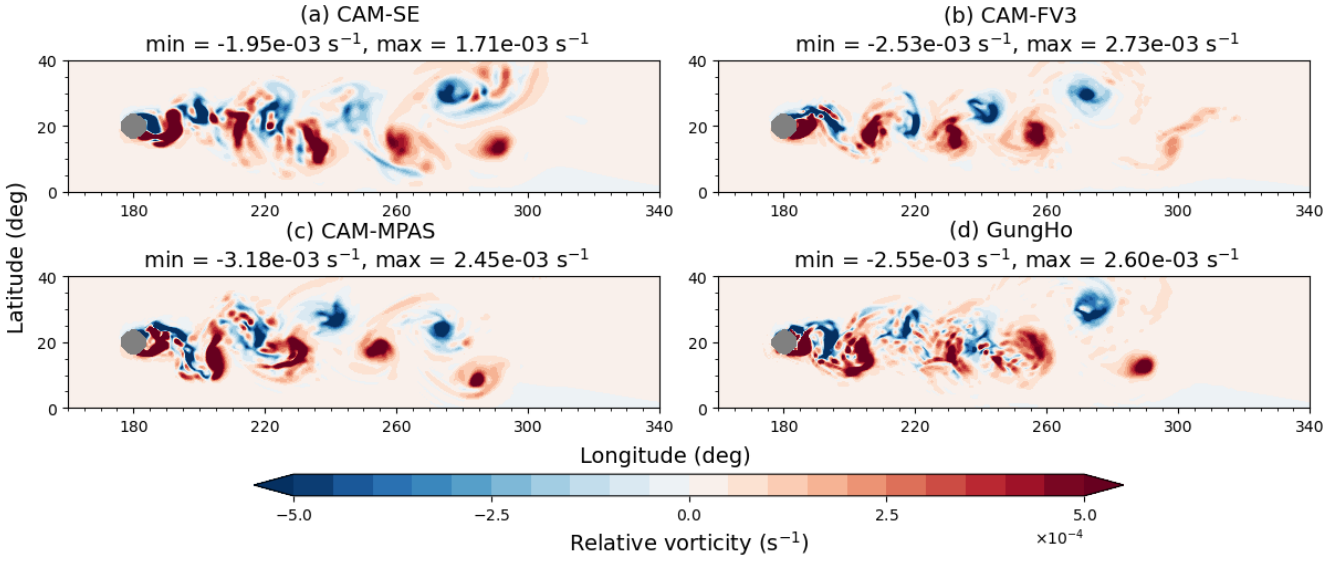

Figure 12. Relative vorticity, ζ, at the end of the vortex shedding test (1 day) *without* rotation, plotted at $z = 300$ m.

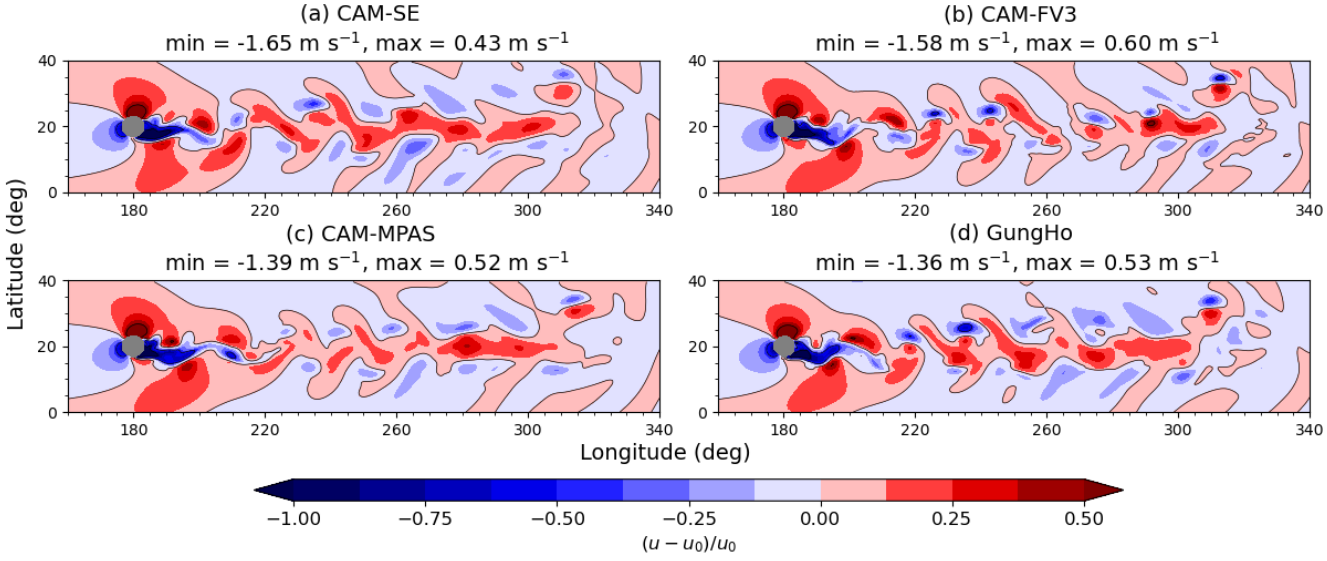

Figure 13. Normalised zonal wind perturbation, u', at the end of the vortex shedding test (1 day) *with* rotation, plotted at $z = 300$ m.

https://doi.org/10.5194/egusphere-2026-2293
Preprint. Discussion started: 24 June 2026

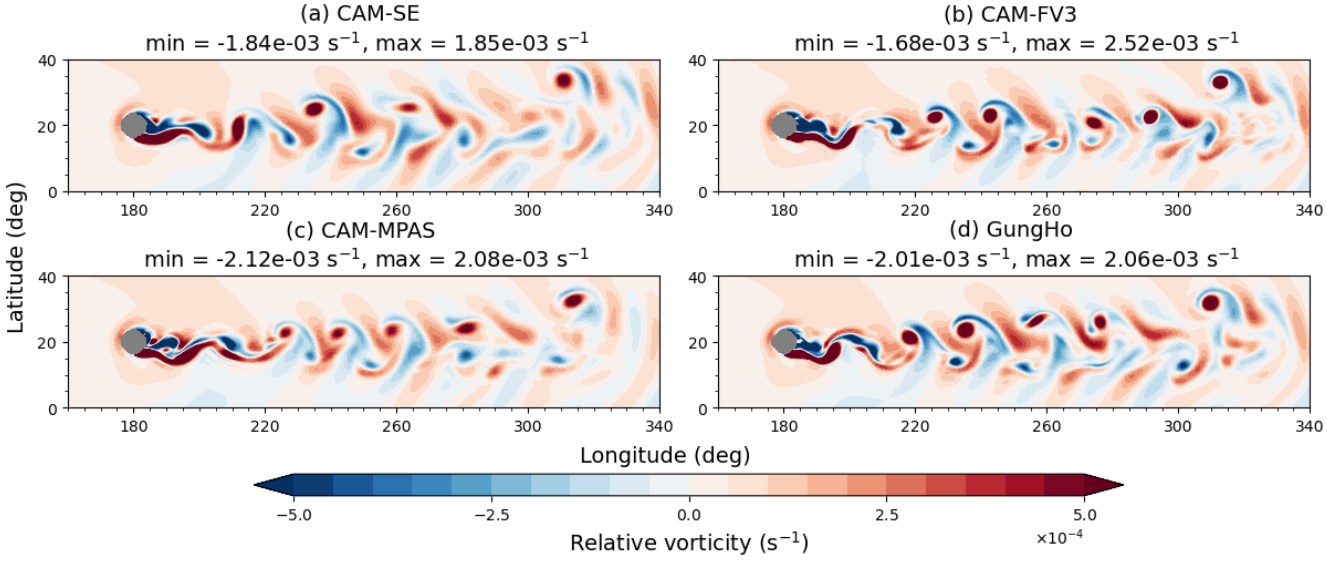

Figure 14. Relative vorticity, ζ, at the end of the vortex shedding test (1 day) *with* rotation, plotted at $z = 300$ m.

https://doi.org/10.5194/egusphere-2026-2293
Preprint. Discussion started: 24 June 2026

6 Diffusion sensitivity analyses

Both the gap flow and vortex shedding variants of this test case are sensitive to diffusion choices within the dynamical core. This section will examine one diffusion mechanism from each dynamical core, although there are many other sources of diffusion that are worth exploration.

6.1 CAM-SE: Hyperdiffusion strength

As noted in the previous sections, the strength of the fourth-order hyperdiffusion in CAM-SE typically leads to smoother dynamics than the other models. We examine this further through reduced hyperdiffusion coefficients, which are half the value of the CAM defaults (see `se_nu`, `se_nu_div`, and `se_nu_p` in Table D1). Figures 15 and 16 show the impact of weaker diffusion on the temperature perturbation field of the gap flow test. For the case without rotation (Figure 15), halving the diffusion strength leads to more small-scale features, and makes the field look closer to that of GungHo (Fig. 6). For the case with rotation (Fig. 16), the shape of the detached lee vortices becomes more circular with weaker diffusion. Intriguingly, reducing the hyperdiffusion strength increases the maximum temperature for the gap flow without rotation, but conversely reduces the maximum temperature when rotation is included.

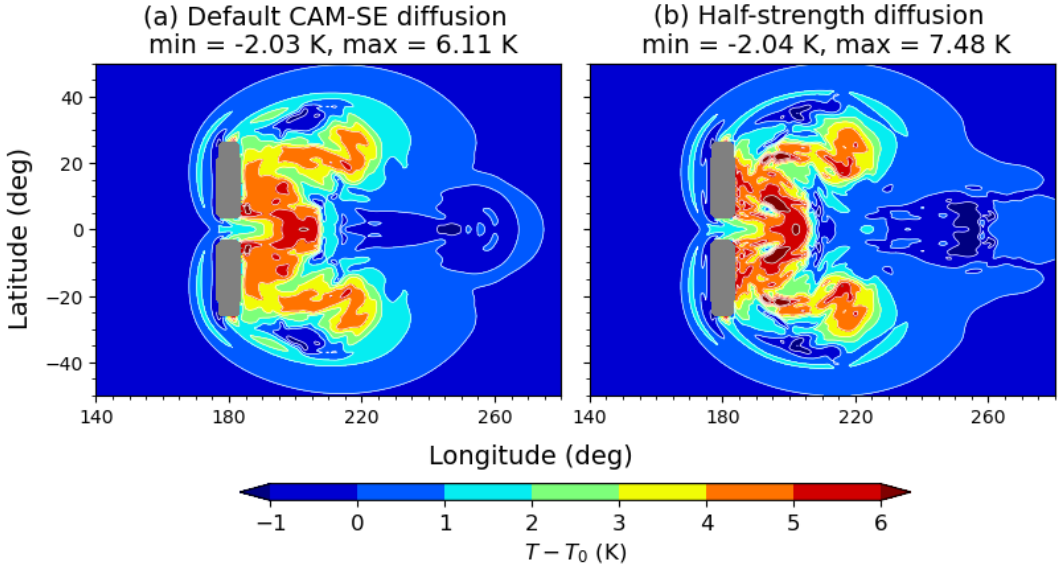

Figure 15. Comparing the temperature perturbation field from CAM-SE at the end of the gap flow test (0.5 days) *without* rotation, with default CAM diffusion (a) and halved hyperdiffusion coefficients (b). A reduced hyperdiffusion strength permits more small-scale features and increases the maximum temperature perturbation downstream of the mountain.

https://doi.org/10.5194/egusphere-2026-2293
Preprint. Discussion started: 24 June 2026

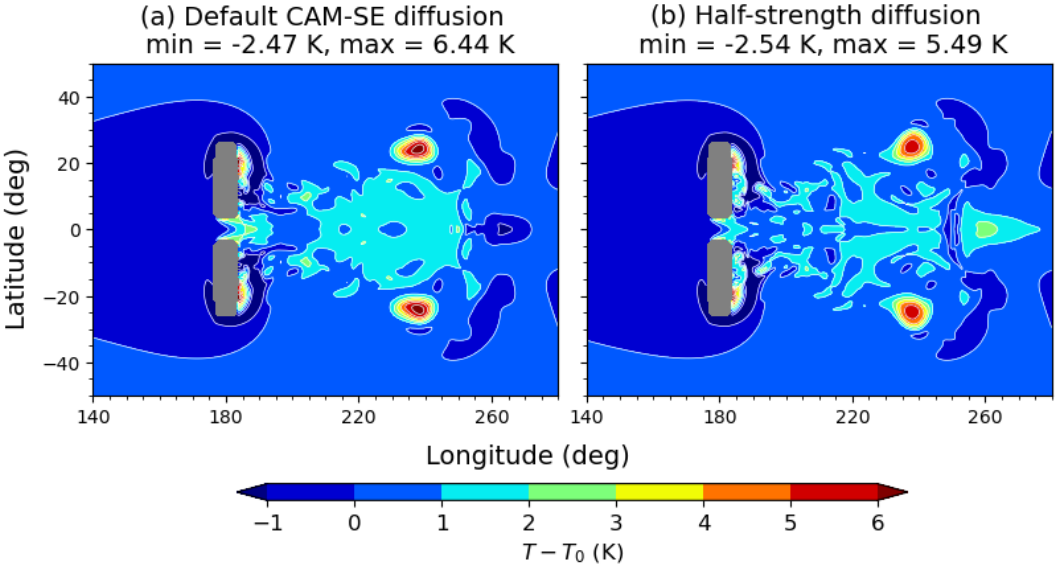

Figure 16. Comparing the temperature perturbation field from CAM-SE at the end of the gap flow test (0.5 days) *with* rotation, with default CAM diffusion (a) and halved hyperdiffusion coefficients (b). Weaker hyperdiffusion changes the shape of the lee vortices and reduces the maximum temperature perturbation downstream of the mountain.

6.2 CAM-FV3: Horizontal transport scheme

The choice of horizontal transport scheme in FV3 impacts the level of implicit diffusion. Whilst all the FV3 transport schemes use the PPM method of Colella and Woodward (1984), there are different limiting options and the ability to apply monotonicity constraints. We compare the default CAM horizontal transport scheme, which applies monotonicity constraints on each transported field, with a virtually inviscid scheme that is 'unlimited' and applies no monotonicity constraints (the `hord` namelist options for the two schemes are listed in Table D2). The virtually inviscid scheme is expected to be much less diffusive than the default CAM transport method.

The two horizontal transport schemes are first compared in the gap flow test without rotation (Fig. 17), with the diminished implicit diffusion of the virtually inviscid scheme leading to a wider temperature perturbation range. Strikingly, the virtually inviscid scheme contains small-scale noise that is not present with default CAM transport and also induces asymmetry in the detached vortices, which is undesirable given FV3's equatorially symmetric gnomonic cubed-sphere grid. We note that the reduced implicit diffusion of the virtually inviscid scheme can be compensated for with a stronger divergence damping coefficient (Table D2), or the addition of other diffusion mechanisms such as vorticity damping.

Figure 18 compares the horizontal transport schemes in the vortex shedding case without rotation, where the virtually inviscid scheme creates a noisier vortex street. Examining a vertical slice over the mountain (Fig. 19) shows that this noise is partly due to the diminished efficacy of the Rayleigh damping with virtually inviscid transport. Hence, the performance of the sponge

https://doi.org/10.5194/egusphere-2026-2293
Preprint. Discussion started: 24 June 2026

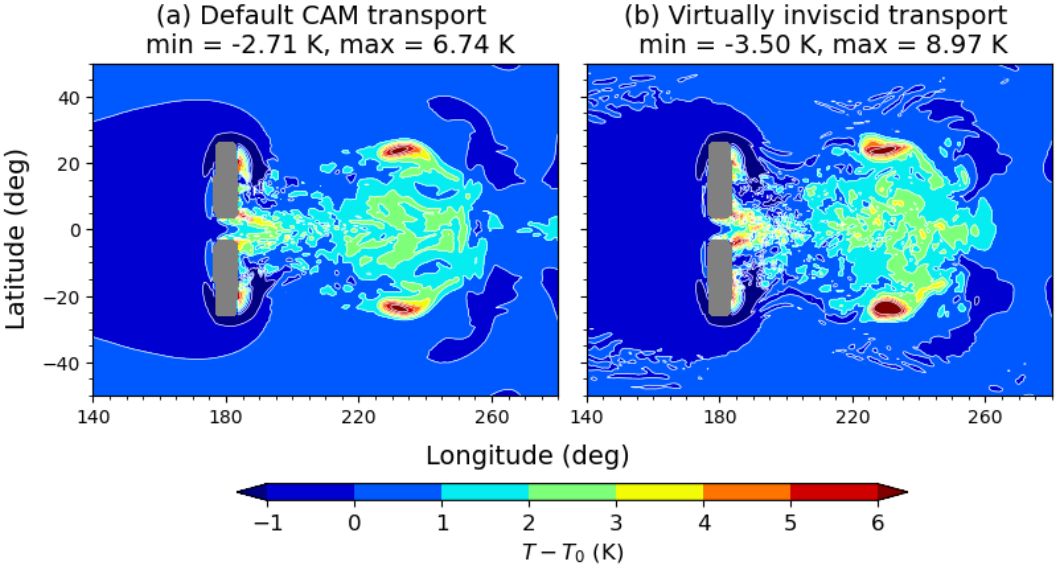

Figure 17. Comparing the temperature perturbation field from CAM-FV3 at the end of the gap flow test (0.5 days) *with* rotation, with default CAM transport (a) and the virtually inviscid transport scheme (b). A wider temperature perturbation range with the virtually inviscid scheme reflects its reduced implicit diffusion.

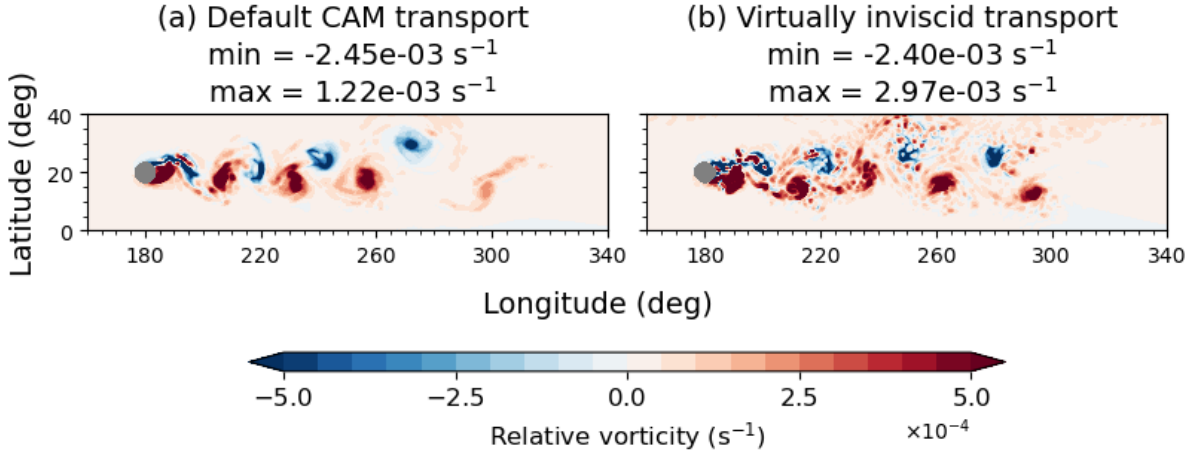

Figure 18. Comparing the relative vorticity field from CAM-FV3 at the end of the vortex shedding test (1 day) *without* rotation, with default CAM transport (a) and virtually inviscid transport (b). The reduced implicit diffusion in the virtually inviscid scheme leads to a noisier vortex street.

layer in minimising reflections can depend on the implicit diffusion of the horizontal transport scheme. Further discussion of the Rayleigh damping layer is given in Appendix C.

https://doi.org/10.5194/egusphere-2026-2293
Preprint. Discussion started: 24 June 2026

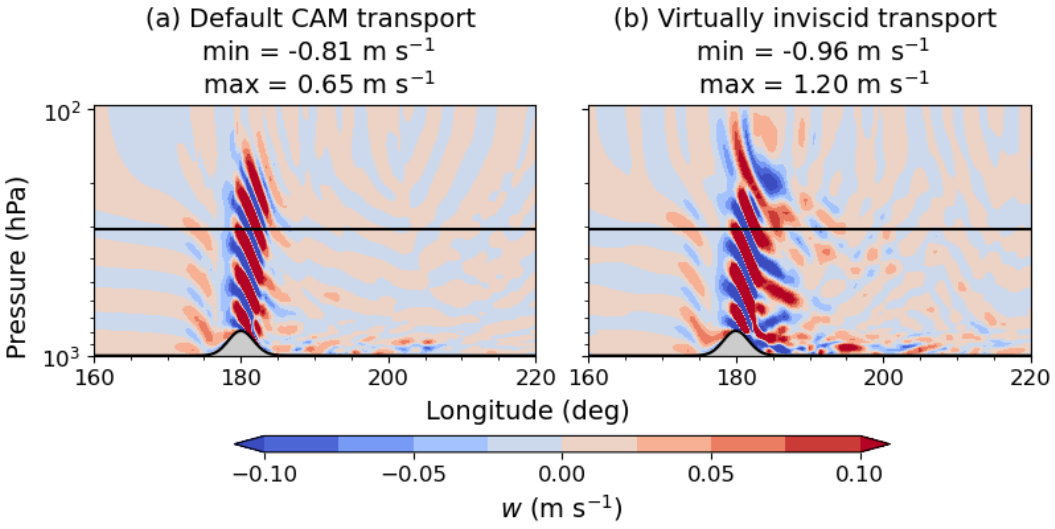

Figure 19. Cross-sections at $\phi = 20^\circ$ of the vertical velocity field ($w = -\omega R_d T/(pg)$ with ω the vertical pressure velocity) in CAM-FV3 at the end of the vortex shedding test (1 day) *without* rotation, with default CAM transport (a) and virtually inviscid transport (b). The same Rayleigh damping sponge layer with $\tau = 100$ s is used with both transport schemes. Whilst the Rayleigh damping sponge successfully avoids reflections of the orographic gravity wave for default CAM transport (a), the use of virtually inviscid transport (b) leads to stronger vertical velocities and reflections that interfere with the vortex street (Figure 18). Note, the colorbar is saturated to more clearly show wave reflections.

6.3 CAM-MPAS: Divergence diffusion strength

The default diffusion option for CAM-MPAS combines Laplacian Smagorinsky diffusion, which varies spatially and temporally based on the local flow deformation, and a fixed-strength fourth-order hyperdiffusion. Like CAM-SE, the fourth-order hyperdiffusion acts on the horizontal velocity and is decomposed into rotational and divergent components, which can be damped by different amounts. The damping of the divergent part is typically ten times stronger than for the rotation part in CAM-MPAS (`mpas_del4u_div_factor` in Table D3). Here, we examine the use of weaker damping of the divergent motions by setting the divergent coefficient equal to the rotational coefficient. In the gap flow test with rotation (Fig. 20), the weaker damping of horizontal divergence leads to a longitudinal stretching of the lee vortices in the temperature field, making them look closer to those of CAM-FV3 and GungHo (Fig. 8). Weaker damping of the divergent part also increases the equatorial asymmetry. In the vortex shedding case with rotation, the weaker divergent diffusion impacts the representation of the rotational vortex dynamics, with stronger and larger cyclonic vortices (Fig. 21). Given that the damping strength of the rotational part is unchanged, this highlights that a model's response to diffusion changes can be complex, with the damping strength of divergent motions impacting the representation of rotational dynamics.

https://doi.org/10.5194/egusphere-2026-2293
Preprint. Discussion started: 24 June 2026

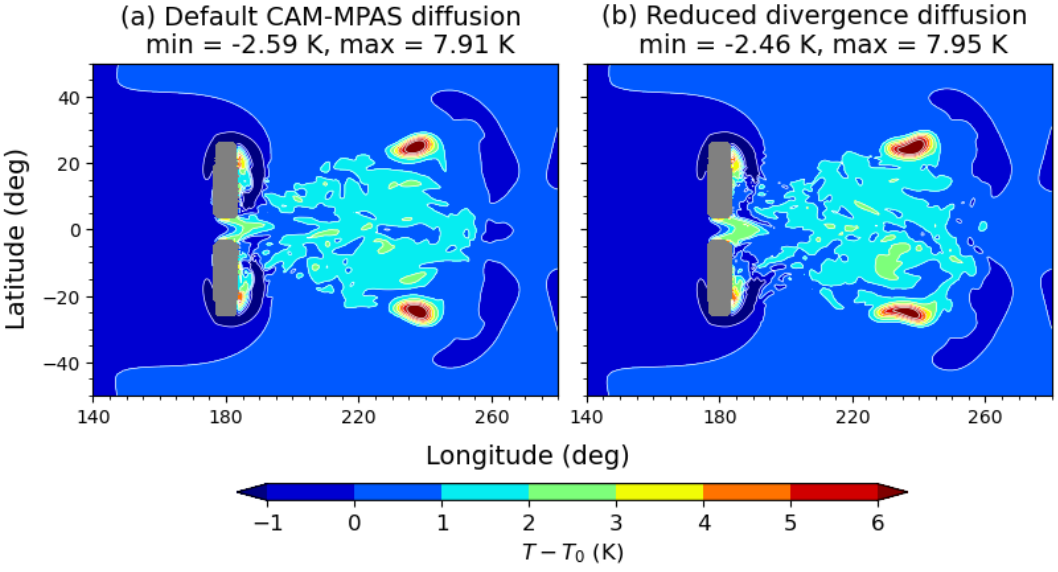

Figure 20. Comparing the temperature perturbation field from CAM-MPAS at the end of the gap flow test (0.5 days) *with* rotation, with default CAM diffusion (a) and a weaker damping of divergent motions (b). Reduced divergence diffusion stretches the lee vortices longitudinally, whilst the range of temperatures remains mainly unchanged.

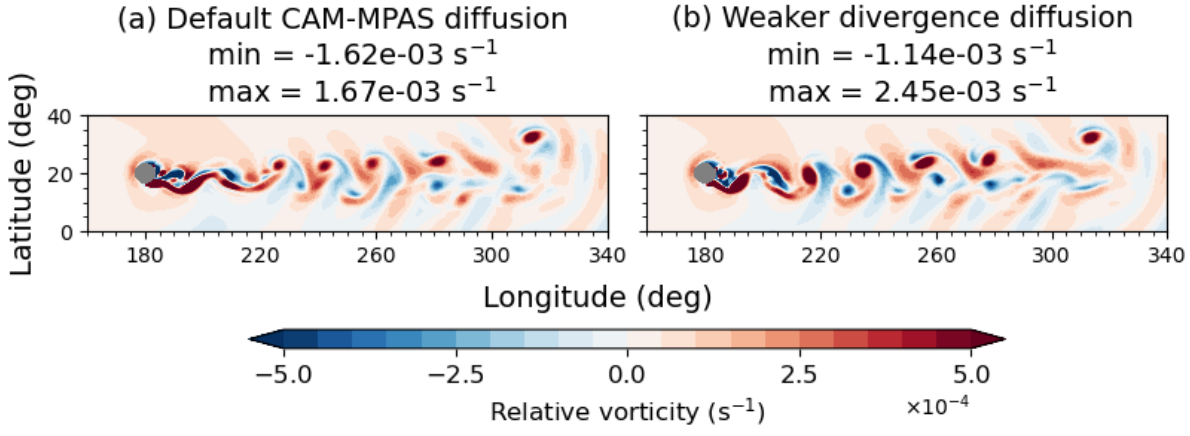

Figure 21. Comparing relative vorticity from CAM-MPAS at the end of the vortex shedding test (1 day) *with* rotation, with default CAM diffusion (a) and a weaker damping of divergent motions (b). Reduced divergence diffusion leads to stronger cyclonic vortices.

https://doi.org/10.5194/egusphere-2026-2293
Preprint. Discussion started: 24 June 2026

6.4 GungHo: Monotonic transport of potential temperature

In GungHo, we examine the use of monotonicity constraints for the transport of the potential temperature, θ. During the development of this test case, instabilities were encountered at coarser vertical resolutions when applying no monotonicity constraint on θ transport. This instability was likely due to the steep slopes of the orography on the small Earth. Whilst the cases presented here with the specified vertical resolution (Appendix B) are stable without monotonicity constraints, this model choice can still impact the simulations. The largest difference is seen in the vortex shedding case without rotation (Fig. 22), with a patchier vortex street without monotonic θ transport. There is a subtler difference for the vortex shedding test with (Fig. 23), with the strongest anticyclonic vortex having a larger magnitude without monotonocity constraints, and there are small differences in the shapes of the cyclonic vortices.

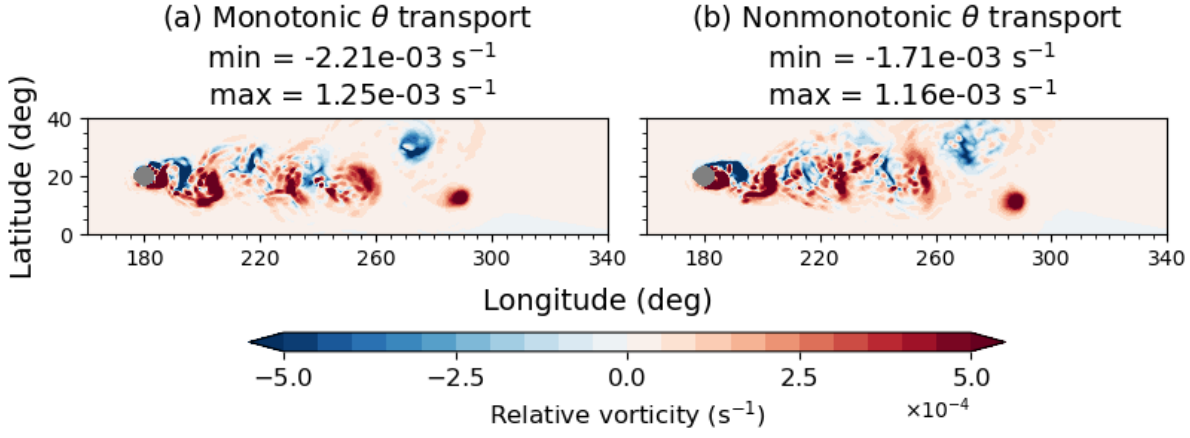

Figure 22. Comparing relative vorticity from GungHo at the end of the vortex shedding test (1 day) *without* rotation, with monotonicity constraints on the potential temperature (a) and without the constraints (b). Removing the monotonicity constraints on θ leads to a patchier vortex street, particularly for the leading anticyclonic vortex.

https://doi.org/10.5194/egusphere-2026-2293
Preprint. Discussion started: 24 June 2026

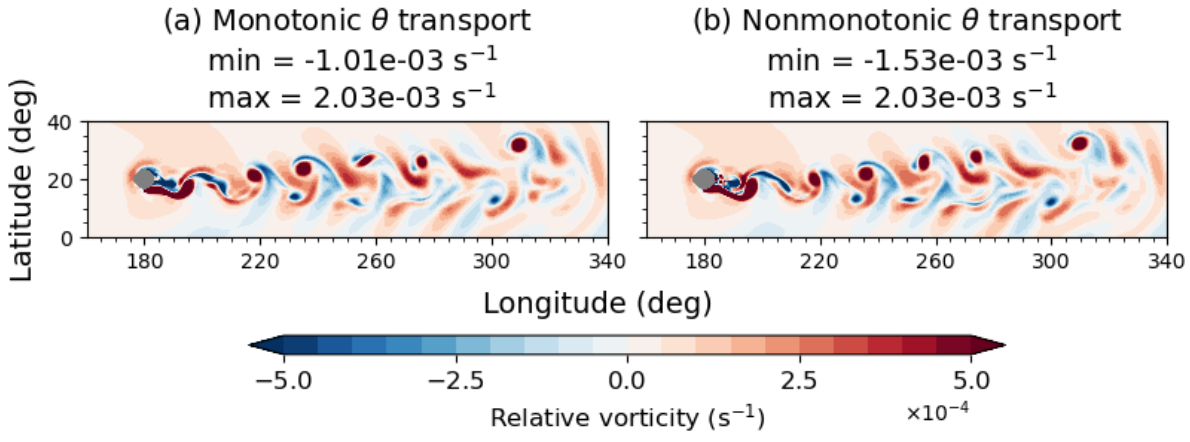

Figure 23. Comparing relative vorticity from GungHo at the end of the vortex shedding test (1 day) *with* rotation, with monotonicity constraints on the potential temperature (a) and without the constraints (b). Removing the monotonicity constraints has no noticeable impact on the largest cyclonic vortex but increases the magnitude of the largest anticyclonic vortex.

https://doi.org/10.5194/egusphere-2026-2293
Preprint. Discussion started: 24 June 2026

7 Conclusions

This paper described a new mountain-generated flow test case, developed for DCMIP-2025, for the evaluation of dynamical cores in atmospheric GCMs. Our test probes how state-of-the-art models represent complex mesoscale phenomena, which is increasingly important as global forecast models pursue finer horizontal resolutions. The simplicity of the initial condition makes this an easy test to implement in a range of numerical models. Whilst two surface height profiles were specifically investigated in DCMIP-2025, with corresponding dynamics of gap flow and vortex shedding, there is scope to develop many other variants of this test case by varying the orography.

Gap flow and vortex shedding simulations with four tested dynamical cores highlighted differences in their model design. Generally, the gnomonic cubed-sphere grids used by CAM-SE, CAM-FV3, and GungHo lead to equatorially symmetric flow in the gap test, whilst the centroidal Voronoi grid in CAM-MPAS permitted asymmetry. Numerical diffusion has a significant impact in the gap flow and vortex shedding tests, so these simulations allow insight about the effect of explicit and implicit diffusion choices. CAM-SE was observed to have the smoothest profiles due to a relatively strong hyperdiffusion, and reducing this permits more small-scale features in its fields. CAM-FV3 is sensitive to the choice of horizontal transport scheme, with the reduced diffusion of the virtually inviscid scheme compared to the default scheme introducing noise and potentially model instability for longer simulations. CAM-MPAS is sensitive to the strength of the damping of divergent motions relative to rotational ones. During testing, the steep mountain slopes on the small Earth revealed the importance of monotonic transport of potential temperature in GungHo, and in stable simulations, the lack of constraints affected the representation of the vortex shedding.

There are a number of modifications that can be made to this test case. A logical next step is the addition of moisture, such as with a Kessler microphysics routine (Kessler, 1969; Hughes and Jablonowski, 2023). The interaction of moisture with steep orography and mesoscale dynamics would provide a tough test for dynamical cores.

For the gap flow case, changes to the gap width and length can instigate different dynamics. The current orography is in the short gap regime, where the gap width is comparable to its length (longitudinal extent). One could instead examine the long gap regime, where the length of the gap is much greater than its width (Stull, 2015). Other orographic modifications include introducing a slope in the gap or adding multiple gaps. Also, varying the flow velocity would impact the inverse Froude number, thus testing dynamical cores in regimes with different compositions of nonlinear and linear dynamics.

For the vortex shedding case, centring the mountain at a different latitude will lead to different vortex streets by changing the zonal velocity differential over the northern and southern slopes. There is also an important relationship between the Strouhal number and the flow Reynolds number, e.g. Nunalee and Basu (2014), that could be studied. Sun and Chern (1994) estimated the Reynolds number from the strength of the explicit Laplacian diffusion, and a similar approach could be used for hyperdiffusive terms, although an effective level of implicit diffusion is harder to quantify. Another possible modification is to the mountain shape, such as using elliptical profiles, like in Sun and Chern (1994).

https://doi.org/10.5194/egusphere-2026-2293
Preprint. Discussion started: 24 June 2026

Code and data availability. Simulations with dynamical cores from the Community Atmosphere Model (CAM) were made using a clone of the publicly available repository at https://github.com/ESCOMP/CAM. The CAM tag numbers used in this work are `cam_6_4_070` for CAM-FV3, `cam_6_4_080` for CAM-MPAS, `cam_6_4_100` for CAM-SE. Initial condition files for CAM-MPAS were constructed using a clone of the MPAS standalone code repository which can be accessed at https://github.com/MPAS-Dev/MPAS-Model. A GitHub respository that contains code from the GungHo dynamical core is found at https://github.com/MetOffice/lfric_apps. Additional scripts used for the CAM simulations and data obtained for the dynamical core comparison figures are archived in the zenodo repository https://zenodo.org/records/19696242 (Andrews et al., 2026). Jupyter notebooks used for making the figures can be found at https://github.com/ta440/DCMIP-2025_gap_and_vortex.

https://doi.org/10.5194/egusphere-2026-2293
Preprint. Discussion started: 24 June 2026

Appendix A: Vertical velocity initialisation for nonhydrostatic models

This appendix derives nonzero vertical velocities for nonhydrostatic models in this test case and evaluates their impact in CAM-MPAS simulations.

We follow the approach of Hughes and Jablonowski (2023) and define an initial condition for w such that a purely horizontal flow is adjusted to follow sloped coordinate lines. This ensures that an impermeability boundary condition is satisfied at the surface (Taylor et al., 2020). The recipe for deriving w follows that in Appendix D of Kent et al. (2014) for hybrid pressure and height coordinates with one key difference: the sign of w is inverted. This is because Kent et al. (2014) was addressing the opposite problem, where a flow defined along sloped coordinate lines was modified to be purely horizontal; see also Appendix B of Ullrich et al. (2012) for a discussion of this *perceived vertical velocity*. Hence, whilst we define an initial w that is positive for $\partial z_\mathrm{s}/\partial\lambda > 0$ and negative for $\partial z_\mathrm{s}/\partial\lambda < 0$ (given positive zonal flow), Kent et al. (2014) and Ullrich et al. (2012) instead define w that is negative for $\partial z_\mathrm{s}/\partial\lambda > 0$ and positive for $\partial z_\mathrm{s}/\partial\lambda < 0$.

To have a flow that follows a sloped vertical coordinate line, s, the vertical velocity is computed as

$$w = \mathbf{u}_H \cdot \boldsymbol{\nabla}_s z. \tag{A1}$$

for $\mathbf{u}_H = [u, v]^T$, and $\boldsymbol{\nabla}_s$ the horizontal gradient operator along sloped coordinate lines. (A1) reduces to $w = 0$ when the vertical coordinate has no horizontal variation, such as a pure height coordinate, or in the absence of orography. For an initial condition of purely zonal flow, the initial vertical velocity is

$$w = \frac{u}{a\cos(\phi)} \frac{\partial z}{\partial \lambda}\bigg|_s, \tag{A2}$$

with $|_s$ denoting the evaluation along sloped coordinate lines. Note that as $a = X^{-1} a_\mathrm{reg}$, the small Earth initial vertical velocities are increased from the regular Earth by a factor of X.

In the case of the hybrid z-coordinate of $z = \overline{z} + A z_\mathrm{s}$, the base grid $\overline{z}$ and blending function A are the same at any horizontal location, so

$$\frac{\partial z}{\partial \lambda} = \frac{\partial}{\partial \lambda}(\overline{z} + A z_\mathrm{s}) = A \frac{\partial z_\mathrm{s}}{\partial \lambda}. \tag{A3}$$

This means that w is proportional to A, so the initial vertical velocity varies with height in a hybrid coordinate, unlike the other components of the initial condition (1).

For the gap flow case, the longitudinal derivative of the orography is

$$\frac{\partial z_\mathrm{s}}{\partial \lambda} = \frac{-e_1}{d_1}\left(\frac{\lambda - \lambda_\mathrm{c}}{d_1}\right)^{e_1 - 1} z_\mathrm{s}, \tag{A4}$$

so the initial vertical velocity is

$$w(\lambda, \phi, z, t = 0) = -\frac{u_0 e_1}{a d_1}\left(\frac{\lambda - \lambda_\mathrm{c}}{d_1}\right)^{e_1 - 1} A z_\mathrm{s}. \tag{A5}$$

https://doi.org/10.5194/egusphere-2026-2293
Preprint. Discussion started: 24 June 2026

For the vortex shedding case,

$$\frac{\partial z_\mathrm{s}}{\partial \lambda} = \frac{\partial z_\mathrm{s}}{\partial r}\frac{\partial r}{\partial \lambda} = \frac{-2r}{d^2}\frac{\partial r}{\partial \lambda} z_\mathrm{s}, \tag{A6}$$

where $\partial r/\partial \lambda$ is redefined to avoid division by zero at the centre of the mountain,

$$\frac{\partial r}{\partial \lambda} = \begin{cases} \dfrac{a\sin(\lambda-\lambda_\mathrm{c})\cos(\phi_\mathrm{c})\cos(\phi)}{\sqrt{1-\cos^2(r/a)}}, & r \neq 0, \\ 0, & r = 0. \end{cases} \tag{A7}$$

The initial vertical velocity for the vortex shedding case is then

$$w(\lambda,\phi,z,t=0) = \begin{cases} -\dfrac{2u_0 r\sin(\lambda-\lambda_\mathrm{c})\cos(\phi_\mathrm{c})\cos(\phi)}{d^2\sqrt{1-\cos^2(r/a)}} A z_\mathrm{s}, & r \neq 0, \\ 0, & r = 0. \end{cases} \tag{A8}$$

Given a blending function $A(z)$ that decreases monotonically with height, the strongest vertical velocities in each vertical column occur at the surface, where $A = 1$. Surface vertical velocities are shown for the gap flow case in Figure A1 and the vortex shedding case in Figure A2. The nonzero initial vertical velocities are restricted to regions of the domain with significant orography, and thus a sloping of the vertical coordinate. Figures A1 and A2 also include cross-sections to show the decay in w with height. The maximum magnitude of the vertical velocity is ± 2.34 m s^{-1} for the gap flow case and ± 1.27 m s^{-1} for the vortex shedding case; these large vertical velocities are a result of the $X = 20$ small Earth.

We now discuss the impact of nonzero vertical velocities in CAM-MPAS simulations for the gap flow case, which has larger initial vertical velocities than the vortex shedding case. Figures A3 and A4 compare fields in simulations without and with rotation, respectively. In both cases, the use of $w \neq 0$ in the initial condition leads to only minor differences in the flow dynamics. Specifically, there remains the same structure of accelerated and decelerated flow in the case without rotation (Figure A3), and the pair of lee vortices are unchanged in the case with rotation (Fig. A4). Hence, even though the magnitude of the initial vertical velocity is quite large around the steep orography on the small Earth, we believe that the approximation of $w(t = 0) = 0$ is reasonable for most nonhydrostatic dynamical cores.

https://doi.org/10.5194/egusphere-2026-2293
Preprint. Discussion started: 24 June 2026

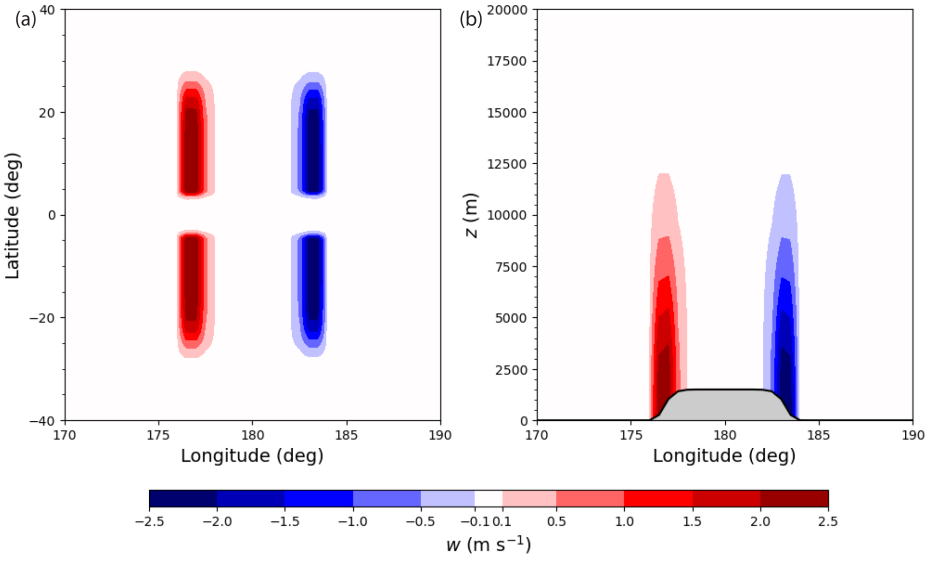

Figure A1. Visualisations of the nonhydrostatic initial vertical velocity in the gap flow test for a hybrid z-coordinate. A section of the surface containing the gap flow orography is shown in (a) and a vertical cross-section at $\phi = 10^\circ$ in (b). The extrema of the vertical velocity field are $w = \pm 2.34$ m s^{-1}. Note that w is positive where the hybrid coordinate slopes upwards, and negative where it slopes downwards.

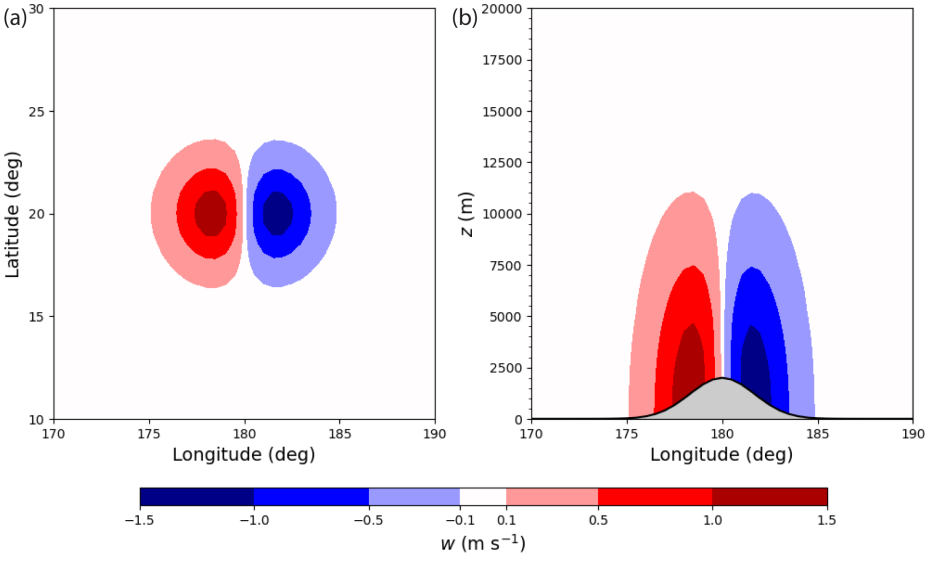

Figure A2. Visualisations of the nonhydrostatic initial vertical velocity in the vortex shedding test for a hybrid z-coordinate. A section of the surface containing the Gaussian mountain is shown in (a) and a vertical cross-section at $\phi = 20^\circ$ in (b). The extrema of the vertical velocity field are $w = \pm 1.27$ m s^{-1}.

https://doi.org/10.5194/egusphere-2026-2293
Preprint. Discussion started: 24 June 2026

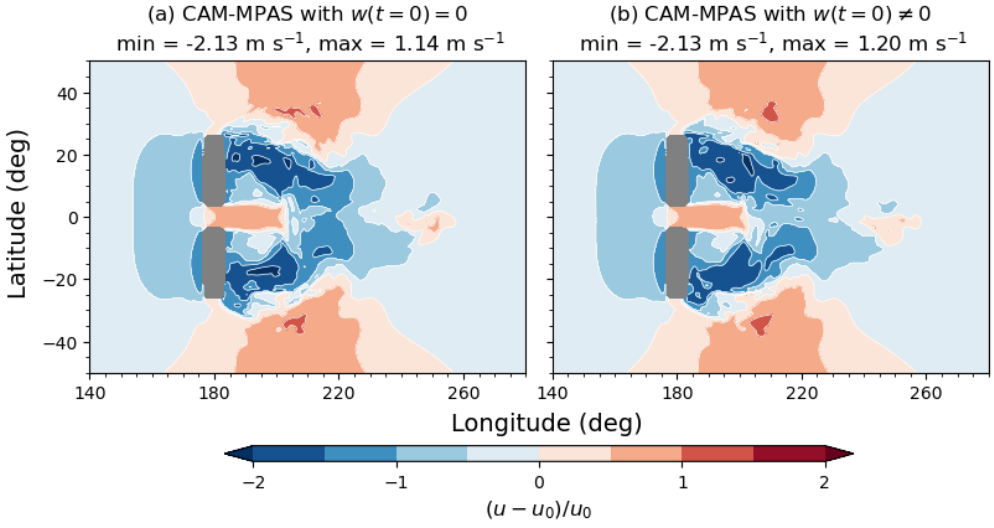

Figure A3. Comparing the normalised velocity field, $u^{'}$ (21), in CAM-MPAS at the end of the gap flow test (0.5 days) without rotation, when using $w(t=0)=0$ (a) and $w(t=0)\neq 0$ (b). There are differences with a nonzero vertical velocity, but the impact on the mesoscale gap flow dynamics is minor.

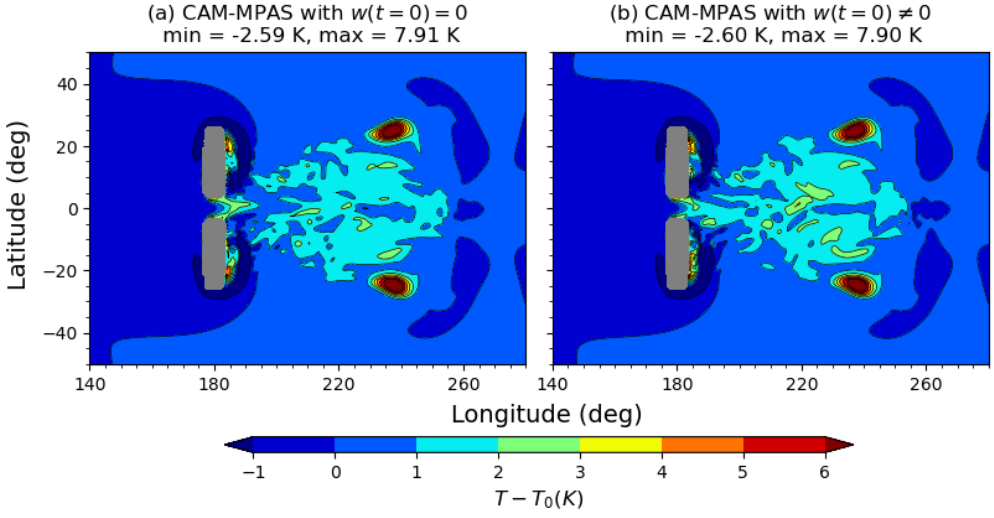

Figure A4. Comparing the temperature perturbation, $T^{'}$ (22), in CAM-MPAS at the end of the gap flow test (0.5 days) with rotation, when using $w(t=0)=0$ (a) and $w(t=0)\neq 0$ (b). There are some small differences in small-scale features when initialising a nonzero vertical velocity, but there is no noticeable impact on the lee vortices.

https://doi.org/10.5194/egusphere-2026-2293
Preprint. Discussion started: 24 June 2026

Appendix B: Vertical grids

This section details the hybrid pressure or height vertical coordinate used by the four dynamical cores. The term 'hybrid' implies a combination of fixed and terrain-following coordinates.

CAM-SE and CAM-FV3 use a hybrid pressure coordinate system of

$$p(\eta) = a(\eta)p_0 + b(\eta)p_\mathrm{s}, \tag{B1}$$

with $a(\eta), b(\eta)$ the hybrid coefficients, p_0 a reference pressure set to 10^5 Pa, and we choose $\eta = p(z)/p_\mathrm{s}$. To compute the hybrid coefficients from a base vertical $\overline{z}$ grid (9, 10), a pressure at each interface $\overline{z}_{k-0.5}$ value is computed using the isothermal relation of

$$p(\overline{z}) = p_0 e^{-\overline{z}/H_\mathrm{iso}}, \tag{B2}$$

with $H_\mathrm{iso} = R_\mathrm{d}T_0/g$ the isothermal scale height. Then, the hybrid coefficients at the interface levels are computed by the method of Laprise and Girard (1990),

$$a_{k-0.5}(\eta) = \eta - b(\eta), \tag{B3a}$$

$$b_{k-0.5}(\eta) = \left(\frac{\eta - \eta_\mathrm{top}}{1 - \eta_\mathrm{top}}\right)^c, \tag{B3b}$$

with $\eta_\mathrm{top} = p(z_\mathrm{T})/p_\mathrm{s}$, for model top z_T. We choose $c = 1$, as recommended by Jablonowski et al. (2008), and set $p_\mathrm{s} = p_0$. Hybrid coefficients at the midpoint levels are then computed as the mean of adjacent interface values,

$$a_k(\eta) = \frac{1}{2}(a_{k-0.5} + a_{k+0.5}), \tag{B4a}$$

$$b_k(\eta) = \frac{1}{2}(b_{k-0.5} + b_{k+0.5}). \tag{B4b}$$

CAM-MPAS and GungHo use a hybrid z-coordinate of the form

$$z = \overline{z} + Az_\mathrm{s}, \tag{B5}$$

where A is a function that blends the orography (z_s) with the fixed height coordinate ($\overline{z}$). The surface orography and a flat model top are enforced by ensuring that $A(\overline{z} = 0) = 1,\ A(\overline{z} = z_\mathrm{T}) = 0$. MPAS uses the blending profile of

$$A(\overline{z}) = \cos^6\left(\frac{\pi}{2}\frac{\overline{z}_k}{z_\mathrm{T}}\right). \tag{B6}$$

Note that MPAS typically performs additional smoothing for complex terrain, as described in Klemp (2011), but this is not required for our orographies where $z_\mathrm{s} \in \mathcal{C}^\infty$. GungHo linearly transitions between terrain-following and flat vertical levels using

$$A(\overline{z}) = \frac{z_\mathrm{T} - \overline{z}}{z_\mathrm{T}}. \tag{B7}$$

https://doi.org/10.5194/egusphere-2026-2293
Preprint. Discussion started: 24 June 2026

As with the hybrid pressure coordinate, the interface $z_{k-0.5}$ levels are first constructed for CAM-MPAS and GungHo, then the midpoint levels are computed through the average

$$z_k = \frac{1}{2}(z_{k+0.5} + z_{k-0.5}). \tag{B8}$$

Appendix C: Discussion of Rayleigh friction

This appendix discusses the use of a Rayleigh friction sponge layer in more depth. An overview of Rayleigh damping in dynamical cores can be found in Jablonowski and Williamson (2011).

There are a number of design choices in constructing the Rayleigh damping layer that can impact its efficacy in minimising wave reflections from the upper boundary. Klemp and Lilly (1978) provides a detailed study of these aspects that was informative for this work. We note that four key choices for the Rayleigh damping layer are:

- **The damping timescale,** τ. This needs to be strong enough to sufficiently damp the waves, but not too strong that the damping layer becomes a source of reflections due to large vertical gradients in the damping coefficient, k_R. Figure C1 demonstrates this balance through three choices of timescale in the gap flow test without rotation. No Rayleigh damping (equivalent to $\tau \to \infty$) permits undamped reflections from the model top, whilst a fast timescale of $\tau = 40$ s leads to reflections from the onset of the Rayleigh damping layer at 10 km. A moderate timescale of $\tau = 100$ s provides a suitable level of damping for the four configurations of this test case.

- **The vertical profile of the damping coefficient,** k_R. The damping coefficient needs to have a smooth vertical variation, as a large value of $dk_R(z)/dz$ or $dk_R(p)/dp$ can instigate reflection from the damping layer itself. Sinusoidal profiles for k_R are common, as used in CAM-FV3 and in this test case (12), (13). Other profiles for the damping coefficient include quadratic (Polvani and Kushner, 2002) or hyperbolic tangent (Zängl et al., 2015) functions, or a linear increase with model level number, as is used for the damping of horizontal velocities in MPAS (Skamarock et al., 2025), although MPAS uses a $\sin^2(z)$ profile for vertical velocity damping.

- **The depth of the sponge layer**. The layer needs to be large enough to sufficiently slow the waves before they hit the model top. Our test uses a 10 km sponge layer, which is approximately equal to $2.90\lambda_z$ at the equator and $2.73\lambda_z$ at 20 degrees North, with λ_z the vertical wavelength of the internal gravity waves (6).

- **The vertical grid spacing in the sponge layer**. A sufficient resolution of the gravity waves is required within the damping layer. With a vertical grid spacing of $\Delta\overline{z} = 500$ m, there is a resolution of 6.9 points per vertical wavelength at the equator, and 6.5 points per vertical wavelength at 20 degrees North.

https://doi.org/10.5194/egusphere-2026-2293
Preprint. Discussion started: 24 June 2026

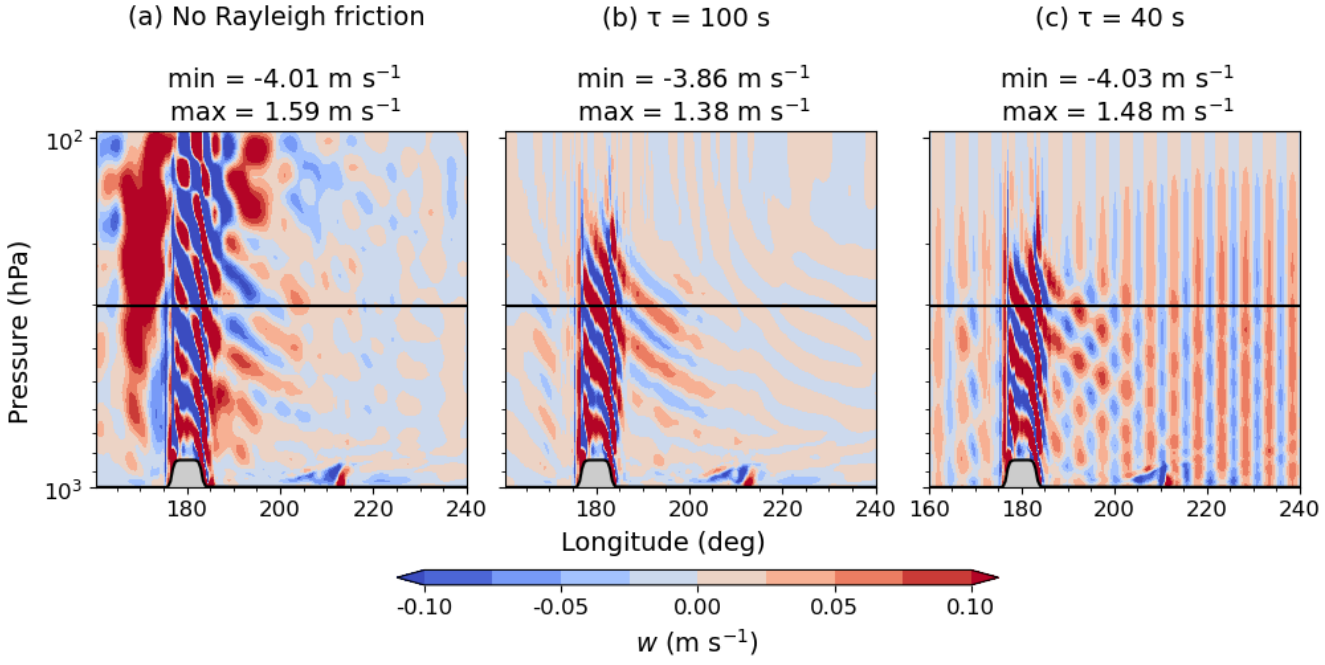

Figure C1. Vertical velocity in a vertical slice of the gap test case without rotation, at a latitude of $\phi = 10^\circ$ and at the end simulation time of 0.5 days. The horizontal black line shows the start of the Rayleigh damping layer at $p_c = 305$ hPa, with the black line at the surface indicating the orography. The CAM-SE dynamical core is used, run with no Rayleigh friction (a), the value used in this paper of $\tau = 100$ s (b), and a stronger damping of $\tau = 40$ s (c). The vertical velocity is computed in an isothermal atmosphere as $w = -\omega R_d T/(pg)$, using prognostic ω, T, p fields, with ω the vertical pressure velocity. Note, the colour range is highly saturated to highlight reflections that may be hidden when plotting a wider range of w values.

With no Rayleigh friction (a), the gravity waves reach the model top unimpeded and there is evidence of reflections of the wave back into the domain. Conversely, making the Rayleigh friction too strong with a short relaxation time (c) leads to reflections from the sponge layer itself; such striped patterns in the vertical velocity are observed just before numerical blow-up when using $\tau < 40$ s. The damping timescale of $\tau = 100$ s (b) successfully damps the wave near the model top and avoids noticeable reflections from either the model top or the damping layer. Using $\tau = 100$ s also leads to a smaller magnitude of the minimum and maximum vertical velocities compared to (a) and (c).

https://doi.org/10.5194/egusphere-2026-2293
Preprint. Discussion started: 24 June 2026

Appendix D: CAM namelist options

Here, we give the key namelist options for the CAM models in Table D1 for CAM-SE, Table D2 for CAM-FV3, and Table D3 for CAM-MPAS. Any modifications to these are made by editing the `user_nl_cam` file. Some general changes for all the CAM dynamical cores are:

- The simulations without rotation require `omega = 0` and the cases with rotation scale the rotation rate through the sidereal day, with `sday = 4308.2`.
- The Rayleigh friction routine in CAM was added by modifying the Held Suarez physics forcing routine. This meant that all models had the additional namelist option of `pertlim = 0.0` to remove initial condition perturbations when using the Held-Suarez compset.
- The $X = 20$ small Earth radius is defined through `rearth = 318561`.

Table D1. Values of the key CAM-SE namelist parameters in this test.

Namelist option	Value
`se_nsplit`	`2`
`se_qsplit`	`1`
`se_rsplit`	`3`
`se_hypervis_subcycle`	`3`
`se_nu`	`1.25E+10` is the scaled default for the $X = 20$ small Earth. `6.25E+9` is used for the reduced (halved) hyperdiffusion test.
`se_nu_div`	`3.125E+10` is the scaled default for the $X = 20$ small Earth. `1.5625E+10` is used for the reduced (halved) hyperdiffusion test.
`se_nu_p`	`1.25E+10` is the scaled default for the $X = 20$ small Earth. `6.25E+9` is used for the reduced (halved) hyperdiffusion test.
`se_nu_top`	`1.0E-10` (effectively switched off)

https://doi.org/10.5194/egusphere-2026-2293
Preprint. Discussion started: 24 June 2026

Table D2. Values of the key CAM-FV3 namelist parameters in this test.

Namelist option	Value
`fv3_k_split`	`2`
`fv3_n_split`	`6`
`fv3_nord`	`2`
`fv3_d2_bg_k1`	`0.0`
`fv3_d2_bg_k2`	`0.0`
`fv3_d2_bg`	`0.0`
`fv3_d4_bg`	`0.15`
`fv3_tau`	`0.0`
`fv3_hord_dp`	`-10` for default CAM transport, `-5` for virtually inviscid transport
`fv3_hord_mt`	`10` for default CAM transport, `5` for virtually inviscid transport
`fv3_hord_tm`	`10` for default CAM transport, `5` for virtually inviscid transport
`fv3_hord_tr`	`8` for default CAM transport, `-5` for virtually inviscid transport
`fv3_hord_vt`	`10` for default CAM transport, `5` for virtually inviscid transport
`fv3_kord_mt`	`9`
`fv3_kord_tm`	`-9`
`fv3_kord_tr`	`9`
`fv3_kord_wz`	`9`

https://doi.org/10.5194/egusphere-2026-2293
Preprint. Discussion started: 24 June 2026

Table D3. Values of the key CAM-MPAS namelist parameters in this test.

Namelist option	Value
mpas_number_of_sub_steps	2
mpas_dynamics_split_steps	3
mpas_dt	22.5
mpas_horiz_mixing	2d_smagorinsky
mpas_smagorinsky_coef	0.125
mpas_mix_full	T
mpas_len_disp	3000.0
mpas_visc4_2dsmag	5.0E-2
mpas_del4u_div_factor	10.0 is the default, 1.0 for weaker divergence diffusion tests
mpas_rayleigh_damp_u	F
mpas_zd	40000.0 (effectively disable vertical velocity damping)
mpas_epssm	0.1
mpas_smdiv	0.1
mpas_w_adv_ord	3
mpas_theta_adv_ord	3
mpas_scalar_adv_ord	3
mpas_w_vadv_ord	3
mpas_theta_vadv_ord	3
mpas_scalar_vadv_ord	3
mpas_scalar_advection	T
mpas_scalar_positive_definite	F
mpas_monotonic	T

https://doi.org/10.5194/egusphere-2026-2293
Preprint. Discussion started: 24 June 2026

Author contributions. TCA, CJ, and OKH developed the test case. TCA and TMB obtained the simulation results and wrote code for the post-processing. TCA made the figures and wrote the paper draft, and TCA and CJ performed edits.

Competing interests. The authors declare that there are no competing interests.

Acknowledgements. Thanks to members of the Atmospheric Dynamics Modeling Group (ADMG) at the University of Michigan for trialing these new test cases for the Dynamical Core Model Intercomparison Project in 2025 (DCMIP-2025). Specifically, thanks to Anthony Chen for writing plotting scripts, and Aaron Johnson, Nicholas Androski, Nicholas Forcone, and Ananyo Bhattacharya for testing the implementation on the Derecho and Casper machines. We would like to acknowledge high-performance computing support from the Derecho (doi:10.5065/qx9a-pg09) and Casper (https://ncar.pub/casper) systems provided by the NSF National Center for Atmospheric Research (NCAR), sponsored by the National Science Foundation (NSF). Thanks to NSF NCAR's Computational and Information Systems Laboratory (CISL) for helping get these test cases running in the presence of technical difficulties during the DCMIP-2025 summer school.

This work was funded by the National Oceanic and Atmospheric Administration (NOAA), grants NA22OAR4320150-T3-01S093 and NA22OAR4590188-T1-01, and the NSF award 2332468.

https://doi.org/10.5194/egusphere-2026-2293
Preprint. Discussion started: 24 June 2026

References

Andrews, T. C. and Jablonowski, C.: Stability analyses of divergence and vorticity damping on gnomonic cubed-sphere grids, arXiv preprint arXiv:2505.05624, 2025.

Andrews, T. C., Jablonowski, C., Bendall, T., and Hughes, O.: Data and Code for "A mountain-generated mesoscale test case from DCMIP-2025: Gap flow and vortex shedding variants", https://doi.org/10.5281/zenodo.19696242, 2026.

Arakawa, A. and Lamb, V. R.: Computational design of the basic dynamical processes of the UCLA general circulation model, Methods in Computational Physics: Advances in Research and Applications, 17, 173–265, 1977.

Bendall, T. M. and Kent, J.: SWIFT: A Monotonic, Flux-Form Semi-Lagrangian Tracer Transport Scheme for Flow with Large Courant Numbers, Mon. Wea. Rev., 2025.

Chen, X.: The LMARS based shallow-water dynamical core on generic gnomonic cubed-sphere geometry, J. Adv. Model. Earth Syst., 13, e2020MS002 280, 2021.

Cherrett, R. C.: Observed and simulated temporal and spatial variations of gap outflow region, Ph.D. thesis, Monterey, CA; Naval Postgraduate School, 2006.

Chopra, K. P. and Hubert, L. F.: Kármán vortex-streets in Earth's atmosphere, Nature, 203, 1341–1343, 1964.

Chopra, K. P. and Hubert, L. F.: Kármán vortex streets in wakes of islands., AIAA Journal, 3, 1941–1943, 1965.

Colella, P. and Woodward, P. R.: The piecewise parabolic method (PPM) for gas-dynamical simulations, J. Comput. Phys., 54, 174–201, 1984.

Colle, B. A. and Mass, C. F.: High-resolution observations and numerical simulations of easterly gap flow through the Strait of Juan de Fuca on 9–10 December 1995, Mon. Wea. Rev., 128, 2398–2422, 2000.

Cotter, C. J. and Shipton, J.: Mixed finite elements for numerical weather prediction, J. Comput. Phys., 231, 7076–7091, 2012.

Dietrich, D. E., Bowman, M. J., Lin, C. A., and Mestas-Nunez, A.: Numerical studies of small island wakes in the ocean, Geophys. Astrophys. Fluid Dyn., 83, 195–231, 1996.

Dong, C. and McWilliams, J. C.: A numerical study of island wakes in the Southern California Bight, Cont. Shelf Res., 27, 1233–1248, 2007.

Dudhia, J.: A nonhydrostatic version of the Penn State–NCAR mesoscale model: Validation tests and simulation of an Atlantic cyclone and cold front, Mon. Wea. Rev., 121, 1493–1513, 1993.

Epifanio, C. and Durran, D.: Lee-vortex formation in free-slip stratified flow over ridges. Part I: Comparison of weakly nonlinear inviscid theory and fully nonlinear viscous simulations, J. Atmos. Sci., 59, 1153–1165, 2002.

Etling, D.: On atmospheric vortex streets in the wake of large islands, Meteorol. Atmospheric Phys., 41, 157–164, 1989.

Gaberšek, S. and Durran, D. R.: Gap flows through idealized topography. Part I: Forcing by large-scale winds in the nonrotating limit, J. Atmos. Sci., 61, 2846–2862, 2004.

Gao, Q., Zeman, C., Vergara-Temprado, J., Lima, D. C., Molnar, P., and Schär, C.: Vortex streets to the lee of Madeira in a kilometre-resolution regional climate model, Weather Clim. Dynam., 4, 189–211, 2023.

Guerra, J. E. and Ullrich, P. A.: A high-order staggered finite-element vertical discretization for non-hydrostatic atmospheric models, Geosci. Model Dev., 9, 2007–2029, 2016.

Harris, L., Chen, X., Putman, W., Zhou, L., and Chen, J.-H.: A scientific description of the GFDL finite-volume cubed-sphere dynamical core, Tech. rep., NOAA GFDL, Princeton, NJ, [Available at https://github.com/NOAA-GFDL/GFDL_atmos_cubed_sphere/blob/main/docs/fv3_technical_2021.pdf], 2021.

https://doi.org/10.5194/egusphere-2026-2293
Preprint. Discussion started: 24 June 2026

Hartney, N., Bendall, T. M., and Shipton, J.: Exploring forms of the moist shallow-water equations using a new compatible finite-element discretisation, Q. J. R. Meteorol. Soc., p. e70018, 2025.

Hong, X., Peng, M., Wang, S., and Wang, Q.: Simulating and understanding the gap outflow and oceanic response over the Gulf of Tehuantepec during GOTEX, Dyn. Atmos. Oceans., 82, 1–19, 2018.

Horváth, Á., Bresky, W., Daniels, J., Vogelzang, J., Stoffelen, A., Carr, J., Wu, D. L., Seethala, C., Günther, T., and Buehler, S.: Evolution of an atmospheric Kármán vortex street from high-resolution satellite winds: Guadalupe Island case study, J. Geophys. Res. Atmos., 125, e2019JD032 121, 2020.

Hubert, L. and Krueger, A.: Satellite pictures of mesoscale eddies, Mon. Wea. Rev., 90, 457–463, 1962.

Hughes, O. K. and Jablonowski, C.: A mountain-induced moist baroclinic wave test case for the dynamical cores of atmospheric general circulation models, Geosci. Model Dev., 16, 6805–6831, 2023.

Huynh, H.: Schemes and constraints for advection, in: Fifteenth International Conference on Numerical Methods in Fluid Dynamics: Proceedings of the Conference Held in Monterey, CA, USA, 24–28 June 1996, pp. 498–503, Springer, 2007.

Jablonowski, C. and Williamson, D. L.: A baroclinic instability test case for atmospheric model dynamical cores, Q. J. R. Meteorol. Soc., 132, 2943–2975, 2006.

Jablonowski, C. and Williamson, D. L.: The pros and cons of diffusion, filters and fixers in atmospheric general circulation models, Numerical techniques for global atmospheric models, pp. 381–493, 2011.

Jablonowski, C., Lauritzen, P., Nair, R., and Taylor, M.: Idealized test cases for the dynamical cores of Atmospheric General Circulation Models: A proposal for the NCAR ASP 2008 summer colloquium, Tech. rep., available online at https://admg.engin.umich.edu/wp-content/uploads/sites/525/2021/03/DCMIP-2008_TestCaseDocument_29May2008.pdf, 2008.

Ju, L., Ringler, T., and Gunzburger, M.: Voronoi tessellations and their application to climate and global modeling, in: Numerical techniques for global atmospheric models, pp. 313–342, Springer, 2011.

Kent, J., Ullrich, P. A., and Jablonowski, C.: Dynamical core model intercomparison project: Tracer transport test cases, Q. J. R. Meteorol. Soc., 140, 1279–1293, 2014.

Kessler, E.: On the distribution and continuity of water substance in atmospheric circulations, in: Meteorological Monographs, pp. 1–84, Springer, 1969.

Kinnmark, I. P. and Gray, W. G.: One step integration methods of third-fourth order accuracy with large hyperbolic stability limits, Math. Comput. Simul., 26, 181–188, 1984.

Klemp, J. and Lilly, D.: Numerical simulation of hydrostatic mountain waves, J. Atmos. Sci., 35, 78–107, 1978.

Klemp, J., Skamarock, W., and Park, S.-H.: Idealized global nonhydrostatic atmospheric test cases on a reduced-radius sphere, J. Adv. Model. Earth Syst., 7, 1155–1177, 2015.

Klemp, J. B.: A terrain-following coordinate with smoothed coordinate surfaces, Mon. Wea. Rev., 139, 2163–2169, 2011.

Konor, C. S. and Randall, D. A.: Impacts of the horizontal and vertical grids on the numerical solutions of the dynamical equations–Part 1: Nonhydrostatic inertia–gravity modes, Geosci. Model Dev., 11, 1753–1784, 2018.

Kuang, Z., Blossey, P. N., and Bretherton, C. S.: A new approach for 3D cloud-resolving simulations of large-scale atmospheric circulation, Geophys. Res. Lett., 32, 2005.

Laprise, R. and Girard, C.: A spectral general circulation model using a piecewise-constant finite-element representation on a hybrid vertical coordinate system, J. Clim., 3, 32–52, 1990.

https://doi.org/10.5194/egusphere-2026-2293
Preprint. Discussion started: 24 June 2026

Lauritzen, P., Conley, A., Lamarque, J.-F., Vitt, F., and Taylor, M.: The terminator "toy" chemistry test: A simple tool to assess errors in transport schemes, Geosci. Model Dev., 8, 1299–1313, 2015.

Lauritzen, P. H., Nair, R. D., Herrington, A., Callaghan, P., Goldhaber, S., Dennis, J., Bacmeister, J., Eaton, B., Zarzycki, C., Taylor, M. A., et al.: NCAR release of CAM-SE in CESM2. 0: A reformulation of the spectral element dynamical core in dry-mass vertical coordinates with comprehensive treatment of condensates and energy, J. Adv. Model. Earth Syst., 10, 1537–1570, 2018.

Lin, S.-J.: A "vertically Lagrangian" finite-volume dynamical core for global models, Mon. Wea. Rev., 132, 2293–2307, 2004.

Lin, S.-J. and Rood, R. B.: Multidimensional flux-form semi-Lagrangian transport schemes, Mon. Wea. Rev., 124, 2046–2070, 1996.

Lin, Y.-L.: Mesoscale dynamics, vol. 10, Cambridge University Press, 2007.

Liu, H., Olsson, P. Q., Volz, K. P., and Yi, H.: A climatology of mesoscale model simulated low-level wind jets over Cook Inlet and Shelikof Strait, Alaska, Estuar. Coast. Shelf Sci., 70, 551–566, 2006.

Liu, Q., Wu, Z., Tan, Z.-M., Yang, F., and Fu, C.: The atmospheric vortex streets and their impact on precipitation in the wake of the Tibetan Plateau, Atmosphere, 14, 1096, 2023.

May, R. M., Goebbert, K. H., Thielen, J. E., Leeman, J. R., Camron, M. D., Bruick, Z., Bruning, E. C., Manser, R. P., Arms, S. C., and Marsh, P. T.: MetPy: A meteorological Python library for data analysis and visualization, Bull. Amer. Meteor. Soc., 103, E2273–E2284, 2022.

Maynard, C., Melvin, T., and Müller, E. H.: Multigrid preconditioners for the mixed finite element dynamical core of the LFRic atmospheric model, Q. J. R. Meteorol. Soc., 146, 3917–3936, 2020.

Mayr, G. J., Armi, L., Gohm, A., Zängl, G., Durran, D. R., Flamant, C., Gaberšek, S., Mobbs, S., Ross, A., and Weissmann, M.: Gap flows: results from the Mesoscale Alpine Programme, Q. J. R. Meteorol. Soc., 133, 881–896, 2007.

Melvin, T., Benacchio, T., Shipway, B., Wood, N., Thuburn, J., and Cotter, C.: A mixed finite-element, finite-volume, semi-implicit discretization for atmospheric dynamics: Cartesian geometry, Q. J. R. Meteorol. Soc., 145, 2835–2853, 2019.

Melvin, T., Shipway, B., Wood, N., Benacchio, T., Bendall, T., Boutle, I., Brown, A., Johnson, C., Kent, J., Pring, S., et al.: A mixed finite-element, finite-volume, semi-implicit discretisation for atmospheric dynamics: Spherical geometry, Q. J. R. Meteorol. Soc., 2024.

Neale, R. B., Chen, C.-C., Gettelman, A., Lauritzen, P. H., Park, S., Williamson, D. L., Conley, A. J., Garcia, R., Kinnison, D., Lamarque, J.-F., et al.: Description of the NCAR community atmosphere model (CAM 5.0), Tech. rep., NCAR, [Available online at https://zerogeoengineering.com/wp-content/uploads/2020/11/cam4_desc.pdf], 2010.

Nunalee, C. G. and Basu, S.: On the periodicity of atmospheric von Kármán vortex streets, Environ. Fluid Mech., 14, 1335–1355, 2014.

Overland, J. E. and Walter Jr, B. A.: Gap winds in the Strait of Juan de Fuca, Mon. Wea. Rev., 109, 2221–2233, 1981.

Park, S.-H., Skamarock, W. C., Klemp, J. B., Fowler, L. D., and Duda, M. G.: Evaluation of global atmospheric solvers using extensions of the Jablonowski and Williamson baroclinic wave test case, Mon. Wea. Rev., 141, 3116–3129, 2013.

Pattiaratchi, C., James, A., and Collins, M.: Island wakes and headland eddies: a comparison between remotely sensed data and laboratory experiments, J. Geophys. Res. Oceans., 92, 783–794, 1987.

Polvani, L. M. and Kushner, P. J.: Tropospheric response to stratospheric perturbations in a relatively simple general circulation model, Geophys. Res. Lett., 29, 18–1, 2002.

Reed, T. R.: Gap winds of the Strait of Juan de Fuca, Mon. Wea. Rev., 59, 373–376, 1931.

Reid, S.: Pressure gradients and winds in Cook Strait, Wea. Forecasting, 11, 476–488, 1996.

Ringler, T. D., Thuburn, J., Klemp, J. B., and Skamarock, W. C.: A unified approach to energy conservation and potential vorticity dynamics for arbitrarily-structured C-grids, J. Comput. Phys., 229, 3065–3090, 2010.

https://doi.org/10.5194/egusphere-2026-2293
Preprint. Discussion started: 24 June 2026

Ronchi, C., Iacono, R., and Paolucci, P. S.: The "cubed sphere": A new method for the solution of partial differential equations in spherical geometry, J. Comput. Phys., 124, 93–114, 1996.

Santos, L. d. F.: Analysis of finite-volume advection schemes on cubed-sphere grids and an accurate alternative for divergent winds, Ph.D. thesis, Universidade de São Paulo, [Avaliable at https://www.teses.usp.br/teses/disponiveis/45/45132/tde-29052024-125153/pt-br.php], 2024.

Schär, C. and Durran, D. R.: Vortex formation and vortex shedding in continuously stratified flows past isolated topography, J. Atmos. Sci., 54, 534–554, 1997.

Schär, C. and Smith, R. B.: Shallow-water flow past isolated topography. Part I: Vorticity production and wake formation, J. Atmos. Sci., 50, 1373–1400, 1993.

Scorer, R. S.: Theory of waves in the lee of mountains, Q. J. R. Meteorol. Soc., 75, 41–56, 1949.

Simmons, A. J. and Burridge, D. M.: An energy and angular-momentum conserving vertical finite-difference scheme and hybrid vertical coordinates, Mon. Wea. Rev., 109, 758–766, 1981.

Skamarock, W. C.: A linear analysis of the NCAR CCSM finite-volume dynamical core, Mon. Wea. Rev., 136, 2112–2119, 2008.

Skamarock, W. C. and Klemp, J. B.: The stability of time-split numerical methods for the hydrostatic and the nonhydrostatic elastic equations, Mon. Wea. Rev., 120, 2109–2127, 1992.

Skamarock, W. C., Doyle, J., Clark, P., and Wood, N.: A standard test set for nonhydrostatic dynamical cores of NWP models, in: AMS NWP-WAF Conference Poster P, vol. 2, 2004.

Skamarock, W. C., Klemp, J. B., Duda, M. G., Fowler, L. D., Park, S.-H., and Ringler, T. D.: A multiscale nonhydrostatic atmospheric model using centroidal Voronoi tesselations and C-grid staggering, Mon. Wea. Rev., 140, 3090–3105, 2012.

Skamarock, W. C., Snyder, C., Klemp, J. B., and Park, S.-H.: Vertical resolution requirements in atmospheric simulation, Mon. Wea. Rev., 147, 2641–2656, 2019.

Skamarock, W. C., Duda, M. G., Klemp, J. B., and Fowler, L.: A Description of the Model for Prediction Across Scales, Atmosphere, Version 8, Tech. rep., NOAA Mesoscale and Microscale Meteorology Laboratory, [Available online at https://www2.mmm.ucar.edu/projects/mpas/mpas_website_linked_files/MPAS-A_tech_note.pdf], 2025.

Smith, R. B.: Comment on "Low Froude number flow past three-dimensional obstacles. Part I: baroclinically generated lee vortices", Journal of Atmospheric Sciences, 46, 3611–3613, 1989a.

Smith, R. B.: Hydrostatic airflow over mountains, in: Advances in geophysics, vol. 31, pp. 1–41, Elsevier, 1989b.

Smolarkiewicz, P. K. and Rotunno, R.: Low Froude number flow past three-dimensional obstacles. Part I: Baroclinically generated lee vortices, J. Atmos. Sci., 46, 1154–1164, 1989.

Steenburgh, W. J., Schultz, D. M., and Colle, B. A.: The structure and evolution of gap outflow over the Gulf of Tehuantepec, Mexico, Mon. Wea. Rev., 126, 2673–2691, 1998.

Stevens, B., Satoh, M., Auger, L., Biercamp, J., Bretherton, C. S., Chen, X., Düben, P., Judt, F., Khairoutdinov, M., Klocke, D., et al.: DYAMOND: the DYnamics of the Atmospheric general circulation Modeled On Non-hydrostatic Domains, Progress in Earth and Planetary Science, 6, 1–17, 2019.

Stull, R. B.: Practical meteorology: an algebra-based survey of atmospheric science, University of British Columbia, 2015.

Sun, W.-Y. and Chern, J.-D.: Numerical experiments of vortices in the wakes of large idealized mountains, J. Atmos. Sci., 51, 191–209, 1994.

Taylor, M., Tribbia, J., and Iskandarani, M.: The spectral element method for the shallow water equations on the sphere, J. Comput. Phys., 130, 92–108, 1997.

https://doi.org/10.5194/egusphere-2026-2293
Preprint. Discussion started: 24 June 2026

Taylor, M. A. and Fournier, A.: A compatible and conservative spectral element method on unstructured grids, J. Comput. Phys., 229, 5879–5895, 2010.

Taylor, M. A., Guba, O., Steyer, A., Ullrich, P. A., Hall, D. M., and Eldred, C.: An energy consistent discretization of the nonhydrostatic equations in primitive variables, J. Adv. Model. Earth Syst., 12, e2019MS001 783, 2020.

Thuburn, J., Ringler, T. D., Skamarock, W. C., and Klemp, J. B.: Numerical representation of geostrophic modes on arbitrarily structured C-grids, J. Comput. Phys., 228, 8321–8335, 2009.

Tomita, H. and Satoh, M.: A new dynamical framework of nonhydrostatic global model using the icosahedral grid, Fluid Dyn. Res., 34, 357–400, 2004.

Tsuchiya, K.: The clouds with the shape of Kármán vortex street in the wake of Cheju Island, Korea, J. Meteor. Soc. Japan, 47, 457–465, 1969.

Ullrich, P. A. and Jablonowski, C.: MCore: A non-hydrostatic atmospheric dynamical core utilizing high-order finite-volume methods, J. Comput. Phys., 231, 5078–5108, 2012.

Ullrich, P. A., Jablonowski, C., Kent, J., Lauritzen, P. H., Nair, R. D., and Taylor, M. A.: Dynamical core model intercomparison project (DCMIP) test case document, Tech. rep., available online at https://public.websites.umich.edu/~cjablono/DCMIP-2012_TestCaseDocument_v1.7.pdf, 2012.

Ullrich, P. A., Melvin, T., Jablonowski, C., and Staniforth, A.: A proposed baroclinic wave test case for deep-and shallow-atmosphere dynamical cores, Q. J. R. Meteorol. Soc., 140, 1590–1602, 2014.

Ullrich, P. A., Jablonowski, C., Reed, K. A., Zarzycki, C., Lauritzen, P. H., Nair, R. D., Kent, J., and Verlet-Banide, A.: Dynamical core model intercomparison project (DCMIP2016) test case document, available online at https://github.com/ClimateGlobalChange/DCMIP2016/blob/master/DCMIP2016-TestCaseDocument_v1.pdf, 2016.

Ullrich, P. A., Jablonowski, C., Kent, J., Lauritzen, P. H., Nair, R., Reed, K. A., Zarzycki, C. M., Hall, D. M., Dazlich, D., Heikes, R., et al.: DCMIP2016: a review of non-hydrostatic dynamical core design and intercomparison of participating models, Geosci. Model Dev., 10, 4477–4509, 2017.

Vallis, G. K.: Atmospheric and oceanic fluid dynamics, Cambridge University Press, 2017.

Wedi, N. P. and Smolarkiewicz, P. K.: A framework for testing global non-hydrostatic models, Q. J. R. Meteorol. Soc., 135, 469–484, 2009.

Wedi, N. P., Polichtchouk, I., Dueben, P., Anantharaj, V. G., Bauer, P., Boussetta, S., Browne, P., Deconinck, W., Gaudin, W., Hadade, I., et al.: A baseline for global weather and climate simulations at 1 km resolution, J. Adv. Model. Earth Syst., 12, e2020MS002 192, 2020.

Wicker, L. J. and Skamarock, W. C.: Time-splitting methods for elastic models using forward time schemes, Mon. Wea. Rev., 130, 2088–2097, 2002.

Williamson, D. L., Olson, J. G., and Jablonowski, C.: Two dynamical core formulation flaws exposed by a baroclinic instability test case, Mon. Wea. Rev., 137, 790–796, 2009.

Willson, J. L., Reed, K. A., Jablonowski, C., Kent, J., Lauritzen, P. H., Nair, R., Taylor, M. A., Ullrich, P. A., Zarzycki, C. M., Hall, D. M., et al.: DCMIP2016: the tropical cyclone test case, Geosci. Model Dev., 17, 2493–2507, 2024.

Wood, N., Staniforth, A., White, A., Allen, T., Diamantakis, M., Gross, M., Melvin, T., Smith, C., Vosper, S., Zerroukat, M., et al.: An inherently mass-conserving semi-implicit semi-Lagrangian discretization of the deep-atmosphere global non-hydrostatic equations, Q. J. R. Meteorol. Soc., 140, 1505–1520, 2014.

Wu, C., Chen, D., Chen, S., Zhang, Y., Su, Q., and Zhang, Y.: Identification of the atmospheric vortex shedding behind the Jeju Island based on MODIS and ERA5 data, Earth and Space Sci., 12, e2024EA004 022, 2025.

https://doi.org/10.5194/egusphere-2026-2293
Preprint. Discussion started: 24 June 2026

Zängl, G.: Stratified flow over a mountain with a gap: Linear theory and numerical simulations, Q. J. R. Meteorol. Soc., 128, 927–949, 2002.

Zängl, G., Reinert, D., Rípodas, P., and Baldauf, M.: The ICON (ICOsahedral Non-hydrostatic) modelling framework of DWD and MPI-M: Description of the non-hydrostatic dynamical core, Q. J. R. Meteorol. Soc., 141, 563–579, 2015.

Zarzycki, C. M., Jablonowski, C., Thatcher, D. R., and Taylor, M. A.: Effects of localized grid refinement on the general circulation and climatology in the Community Atmosphere Model, J. Clim., 28, 2777–2803, 2015.

Zarzycki, C. M., Jablonowski, C., Kent, J., Lauritzen, P. H., Nair, R., Reed, K. A., Ullrich, P. A., Hall, D. M., Taylor, M. A., Dazlich, D., et al.: DCMIP2016: the splitting supercell test case, Geosci. Model Dev., 12, 879–892, 2019.